Influence of floating bridge motion and wind loads on bus users' ride comfort and motion sickness

Citation for the original published paper (version of record):
Sekulic, D., Vdovin, A., Jacobson, B. et al (2025). Influence of floating bridge motion and wind loads on bus users' ride comfort and motion
sickness. Journal of Wind Engineering and Industrial Aerodynamics, 262.
http://dx.doi.org/10.1016/j.jweia.2025.106101

Journal of Wind Engineering & Industrial Aerodynamics 262 (2025) 106101

Contents lists available at ScienceDirect

Journal of Wind Engineering & Industrial Aerodynamics

journal homepage: www.elsevier.com/locate/jweia

Influence of floating bridge motion and wind loads on bus users' ride comfort and motion sickness

Dragan Sekulic [a,*], Alexey Vdovin [a], Bengt Jacobson [a], Simone Sebben [a], Stian Moe Johannesen [b]

[a] Chalmers University of Technology, Gothenburg, Sweden
[b] The Norwegian Public Road Administration, Oslo, Norway

A R T I C L E I N F O

Keywords:
Coach modelling
Bus users
Floating bridge
Wind loads
Ride comfort
Motion sickness
Simulation

A B S T R A C T

Bus users (drivers and passengers) are exposed to vibrations during a journey. Vibration exposure can cause motion sickness, impair ride comfort, and even impact health. Road roughness is the primary source of vehicle vibration. Combined with floating bridge motions, wind loads and high vehicle speeds, the negative vibrational effects can be intensified. This paper investigates the influence of Bjørnafjorden floating bridge motions and wind excitations on bus users' ride comfort and motion sickness for several weather storm conditions. A 13-degree-of-freedom (DOF) intercity bus model with a driver and three passengers was defined for this analysis. The results showed that wind excitations and storm conditions severity significantly affect vehicle velocities at which ISO 2631/1997 ride comfort limits (*a little uncomfortable* and *fairly uncomfortable*) are reached. The passenger in the middle of the bus feels the most comfortable whereas the passenger in the rear part of the bus the least comfortable. The highest value of motion sickness incidence for every user is achieved for the lowest bus speed of 36 km/h due to the longest time of vibrational exposure. Among users, the driver is the most likely to feel motion sickness on a floating bridge due to his suspended seat.

1. Introduction

During a journey, a bus is excited by vibrations from various sources, such as road roughness, aerodynamic loads, wheel imbalance, driving unit, etc. These could impair bus users' ride comfort and even their health in the case of intensive and repetitive shocks (Bowrey et al., 1996; Aslan et al., 2005). Low-frequency vibrations can cause motion sickness, especially over long vibrational exposure, particularly bus drivers can suffer from musculoskeletal disorders (Alperovitch-Najenson et al., 2010; Patterson et al., 1986). Negative vibrational effects from prolonged exposure can influence bus drivers' driving ability and lead to traffic safety issues.

The primary source of vehicle vibration is road roughness. These can be intensified when a vehicle runs across floating bridges. In combination with high vehicle velocities and high wind speeds, the vibration loads on vehicles become important to access comfort and safety. High-tech constructions such as subsea road tunnels and floating and suspension bridges are planned on route E39 to overcome massive fjords within Norway's Coastal Highway road project (Vegvesen, 2017). Reconstructed ferry-free route E39 will connect the south and north parts of Norway country (Fig. 1). The improved route will enable higher average vehicle velocities and reduced journey time between Kristiansand and Trondheim (from 21 to 11 h). A floating bridge is planned for Bjørnafjorden (Fig. 1a), and a straight concept solution is presented in Fig. 1b.

Several studies deal with the vibrational influence on ride comfort of bus users on stationary roads (Sekulic et al., 2013, 2016; Blood et al., 2010). Ride comfort and allowable vibrational exposure time for an intercity bus driver and two passengers on an asphalt-concrete road in good condition have been investigated in (Sekulic et al., 2013). The bus model of 10 DOF was moving along a straight line only at a constant speed of 100 km/h. Only vertical vibrations from the bus users' seats were considered in the comfort analysis. It was concluded that vibration from the passenger seat in the rear part of the bus influenced the ride comfort. A few studies investigate the vibrational influence of environmental excitations on vehicle users when driving across long-span

* Corresponding author. Chalmers University of Technology, Gothenburg, Sweden.
E-mail addresses: dragan.sekulic@chalmers.se, d.sekulic@sf.bg.ac.rs (D. Sekulic), alexey.vdovin@chalmers.se (A. Vdovin), bengt.jacobson@chalmers.se (B. Jacobson), simone.sebben@chalmers.se (S. Sebben), stian.moe.johannesen@vegvesen.no (S.M. Johannesen).

https://doi.org/10.1016/j.jweia.2025.106101
Received 3 July 2024; Received in revised form 26 March 2025; Accepted 1 April 2025
Available online 9 April 2025

bridges. Driver ride comfort of three vehicle types (heavy truck of 19 DOF; light truck and light car, both of 11 DOF) on a long-span bridge was numerically investigated in (Zhou and Chen, 2016). The ride comfort assessment considered the influence of stochastic traffic flow on the bridge and wind excitations. Yaw acceleration at the driver seat was not considered when assessing comfort by standard ISO 2631/1997. It was confirmed that the lateral and roll accelerations were the most influenced by the wind loads. Traffic flow on the bridge only affects the ride comfort of light truck drivers. The driver ride comfort of light truck and sedan car (both of 13 DOF) on slender coastal bridges under the influence of the lateral wind and wave excitations was numerically analysed in (Zhu et al., 2018). It was revealed that the wave load had insignificant effects on ride comfort compared to the wind load for both vehicles. Ride comfort for drivers of four types of vehicles (sedan car, minivan, motor bus and truck) in stochastic traffic flow on a long-span bridge under vortex-induced vibration was investigated in (Zhu et al., 2021). It was concluded that bus driver's ride comfort gets worse with the lower quality of road roughness. Bus driver's comfort is also affected by the density of traffic flow and the proportion of heavy vehicles. Investigations of intercity bus users' ride comfort, especially their motion sickness on floating bridges under the influence of wind excitations, are missing.

Two methods are employed, either independently or in combination, to measure passenger comfort in the means of public transportation. First one is objective method based on measuring kinematic values (e.g. accelerations), and second one is subjective method for evaluation of passenger comfort perception (e.g. using questionnaires). Ride comfort zones had been defined for an intercity bus in an objective investigation (Sekulic et al., 2016). Simulations confirmed that oscillatory zones with different comfort assessments exist in the bus depending on road quality and vehicle velocity. A subjective method was employed in (Shen et al., 2016). The method considered two-day survey of bus passenger perception in Harbin during peak and off-peak hours. Ride comfort was evaluated by passenger load factor and in-vehicle time. The study results shown that as the comfort perception score increases, the in-vehicle time and degree of congestion (passenger load factor) increase for both seated and standing passengers. On-board comfort level combining subjective and objective methods had been defined in (Barabino et al., 2019). This methodology determines a comfort domain and accurately identifies the areas where passengers experience comfort/discomfort related to bus drivers' driving styles.

The first aim of this paper is to define a mathematical coach model appropriate for investigating vibration effects caused by environmental excitations (road roughness, bridge motions and wind) on bus users' responses. The second goal is to analyse the influence of wind excitations for 1-year storm condition on the intercity bus driver and passengers' ride comfort and motion sickness. The third aim is to investigate the influence environmental excitations for different storm conditions (i.e. storms of lower and higher intensity than 1-year) on the intercity bus users' ride comfort and motion sickness. The final goal is to determine the bus velocity at which ISO 2631/1997 ride comfort and motions sickness limits on the floating bridge are reached for every bus user. Knowing the comfort limits velocity could help ensure a good driver's working ability and reliable transport along the route. To accomplish these aims, a mathematical bus model of 13 DOF is defined. The bus model incorporates four point masses representing a driver and three passengers seated at different parts of the bus body. Ride comfort and motion sickness were assessed using the methodology proposed by the international standard ISO 2631/1997 (ISO 2631, 1997). Bus modelling and numerical simulations were performed using MATLAB/Simulink software.

2. VEHICLE and driver models

In this section, the mathematical coach model is described by differential equations of motion (EOM) applying the method of Newton's second law for translational motions and D'Alembert's principle for angular motions. The driver model is also briefly presented.

2.1. Coach mathematical model definition

A vehicle model defined in this paper is based on the 8 DOF coach model previously defined in (Sekulic et al., 2021). The baseline 8 DOF bus model was used for the analysis of its dynamic behaviour and safe speed determination on the Bjørnafjorden floating bridge under different weather conditions (Sekulic et al., 2021, 2023). In-road-plane DOFs include bus lateral (y) and yaw motion (ψ) (Fig. 2a), whereas out-of-road-plane DOFs include vertical and roll motions of the bus sprung mass and unsprung masses (front and rear axle) (z, z_1, z_2, φ_s, φ_{x1}, φ_{x2}) (Fig. 2b). For the purpose of ride comfort and motion sickness analysis, the baseline model is modified and extended with five out-of-road-plane DOFs – pitch motion of the bus body (θ_s) and vertical motions of four bus users (a driver and three passengers (z_d, z_{p1}, z_{p2}, z_{p3}), Fig. 2b. Notifications are presented in Fig. 2, and Appendix (Tables 3 and 4) contains their values. Values are taken from the literature (Sekulic et al., 2021; Juhlin, 2009; William et al., 2014; Jacobson, 2020). Applied

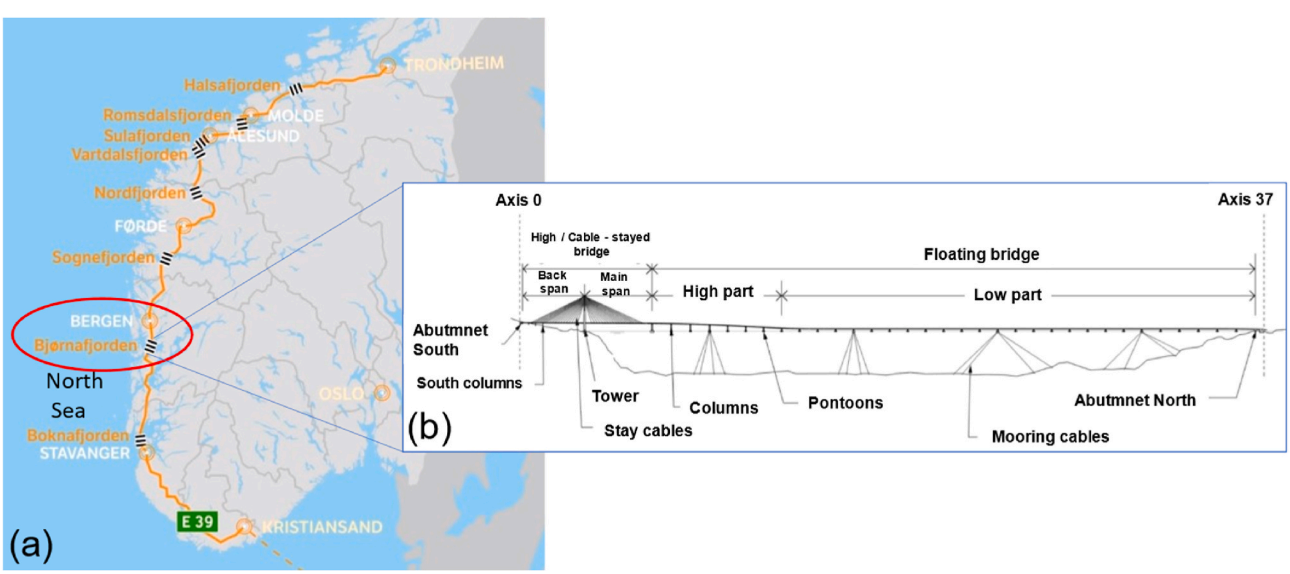

Fig. 1. E39 route in Norway a) Bjørnafjorden; b) straight floating bridge (Vegvesen, 2017).

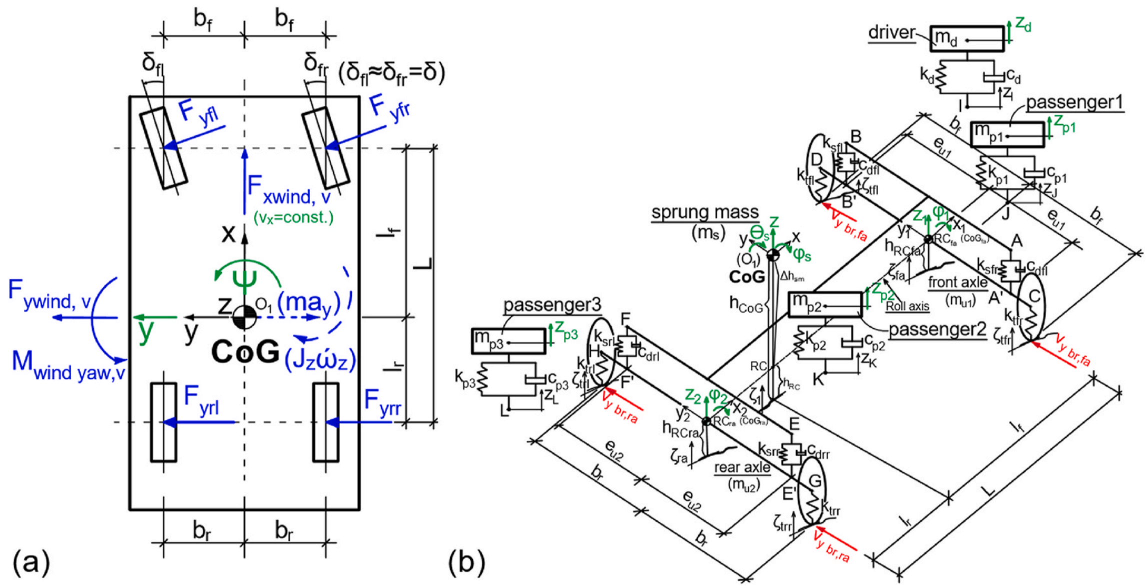

Fig. 2. Bus model a) in-road-plane DOFs; b) out-of-road-plane DOFs.

assumptions when forming a coach model are the same ones as in (Sekulic et al., 2021).

Fig. 3 shows the positions of the bus users' seats considered in the analysis. To determine seat positions, the intercity bus Volvo 9700 is used. Driver's and passenger1's seats are located in the bus front overhang, passenger2's seat is located in the middle part of the bus and passenger3's seat is located in the bus rear overhang. Longitudinal and lateral distances of the bus users' seats ($s_{1\text{-}8}$) with respect to bus CoG are denoted in Fig. 3. Basic bus geometric parameters (wheelbase, front and rear overhang) are also marked in Fig. 3.

2.1.1. EOMs for in-road-plane DOFs

EOMs for in-road-plane DOFs are the same form as in (Sekulic et al., 2021) and described by Eqs. (1) and (2)

$$m(\dot{v}_y + v_x\omega_z) = F_{yfl}\cos\delta + F_{yfr}\cos\delta + F_{yrl} + F_{yrr} + F_{ywind,v} \tag{1}$$

$$J_z\dot{\omega}_z = (F_{yfl} - F_{yfr})\sin\delta b_f + (F_{yfl} + F_{yfr})\cos\delta l_f - (F_{yrl} + F_{yrr})l_r + M_{wind\ yaw,v} \tag{2}$$

where F_{yfl}, F_{yfr} are lateral tyre forces for the front left/right wheel (Fig. 2a); F_{yrl}, F_{yrr} are lateral tyre forces for the rear left/right wheel (Fig. 2a); $F_{ywind,v}$ and $M_{wind\ yaw,v}$ are lateral component of the wind force and wind yawing moment (Fig. 2a), respectively. Lateral tyre forces are described by the brush tyre model given by Eq. (25) in (Sekulic et al., 2022).

2.1.2. EOMs for out-of-road-plane DOFs

Fig. 4 shows a free-body diagram (FBD) of a bus user's body lumped with the seat with active and fictive forces acting on it. The weight of the human body and a seat is not considered an active force since the

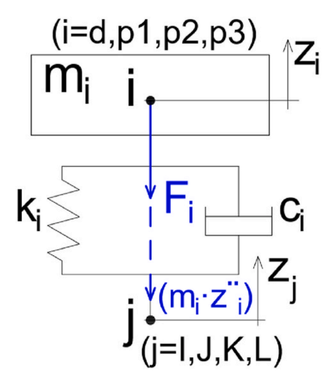

Fig. 4. FBD of bus users' bodies with their seats.

coordinate system for the vertical motion of each point mass is placed in its static position.

The magnitudes of the seat forces for driver, passenger1, passenger2 and passenger3 are given by Eqs. (3)–(6)

$$F_d = k_d(z_d - z_I) + c_d\left(\dot{z}_d - \dot{z}_I\right) = k_d(z_d - z + \theta_s s_2 - \varphi_s s_1) + c_d\left(\dot{z}_d - \dot{z} + \dot{\theta}_s s_2 - \dot{\varphi}_s s_1\right) \tag{3}$$

$$F_{p1} = k_{p1}(z_{p1} - z_J) + c_{p1}\left(\dot{z}_{p1} - \dot{z}_J\right) = k_{p1}(z_{p1} - z + \theta_s s_4 + \varphi_s s_3) + c_{p1}\left(\dot{z}_{p1} - \dot{z} + \dot{\theta}_s s_4 + \dot{\varphi}_s s_3\right) \tag{4}$$

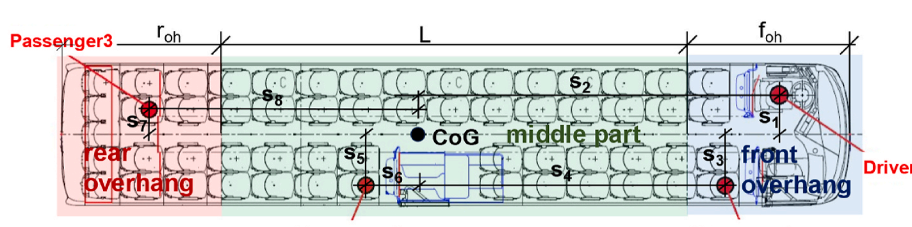

Fig. 3. Intercity bus Volvo 9700 with bus users' seats.

$$F_{p2} = k_{p2}\left(z_{p2} - z_K\right) + c_{p2}\left(\dot{z}_{p2} - \dot{z}_K\right) = k_{p2}\left(z_{p2} - z - \theta_s s_6 + \varphi_s s_5\right) + c_{p2}\left(\dot{z}_{p2} - \dot{z} - \dot{\theta}_s s_6 + \dot{\varphi}_s s_5\right) \tag{5}$$

$$F_{p3} = k_{p3}\left(z_{p3} - z_L\right) + c_{p3}\left(\dot{z}_{p3} - \dot{z}_L\right) = k_{p3}\left(z_{p3} - z - \theta_s s_8 - \varphi_s s_7\right) + c_{p3}\left(\dot{z}_{p3} - \dot{z} - \dot{\theta}_s s_8 - \dot{\varphi}_s s_7\right) \tag{6}$$

Differential EOMs for vertical direction for driver, passenger1, passenger2 and passenger3 are given by Eqs. (7)–(14)

$$m_d \ddot{z}_d = -F_d \tag{7}$$

$$m_d \ddot{z}_d = -c_d \dot{z}_d - k_d z_d + c_d \dot{z} + k_d z + c_d s_1 \dot{\varphi}_s + k_d s_1 \varphi_s - c_d s_2 \dot{\theta}_s - k_d s_2 \theta_s \tag{8}$$

$$m_{p1} \ddot{z}_{p1} = -F_{p1} \tag{9}$$

$$m_{p1} \ddot{z}_{p1} = -c_{p1} \dot{z}_{p1} - k_{p1} z_{p1} + c_{p1} \dot{z} + k_{p1} z - c_{p1} s_3 \dot{\varphi}_s - k_{p1} s_3 \varphi_s - c_{p1} s_4 \dot{\theta}_s - k_{p1} s_4 \theta_s \tag{10}$$

$$m_{p2} \ddot{z}_{p2} = -F_{p2} \tag{11}$$

$$m_{p2} \ddot{z}_{p2} = -c_{p2} \dot{z}_{p2} - k_{p2} z_{p2} + c_{p2} \dot{z} + k_{p2} z - c_{p2} s_5 \dot{\varphi}_s - k_{p2} s_5 \varphi_s + c_{p2} s_6 \dot{\theta}_s + k_{p2} s_6 \theta_s \tag{12}$$

$$m_{p3} \ddot{z}_{p3} = -F_{p3} \tag{13}$$

$$m_{p3} \ddot{z}_{p3} = -c_{p3} \dot{z}_{p3} - k_{p3} z_{p3} + c_{p3} \dot{z} + k_{p3} z + c_{p3} s_7 \dot{\varphi}_s + k_{p3} s_7 \varphi_s + c_{p3} s_8 \dot{\theta}_s + k_{p3} s_8 \theta_s \tag{14}$$

Fig. 5 presents FBDs of the coach sprung mass and front/rear axle with active and fictive forces acting on them. The weights of the bus body and axles are not considered active forces as the coordinate systems for the vertical motions are placed in their static positions.

Magnitudes of forces from the bus suspension system on the front left/right side and rear left/right side are presented by Eqs.(15)–(18)

$$F_{sfl} = k_{sfl}(z_B - z_{B'}) + c_{dfl}\left(\dot{z}_B - \dot{z}_{B'}\right) = k_{sfl}\left(z - \theta_s l_f + e_{u1}\varphi_s - z_1 - e_{u1}\varphi_1\right) + c_{dfl}\left(\dot{z} - \dot{\theta}_s l_f + e_{u1}\dot{\varphi}_s - \dot{z}_1 - e_{u1}\dot{\varphi}_1\right) \tag{15}$$

$$F_{sfr} = k_{sfr}(z_A - z_{A'}) + c_{dfr}\left(\dot{z}_A - \dot{z}_{A'}\right) = k_{sfr}\left(z - \theta_s l_f - e_{u1}\varphi_s - z_1 + e_{u1}\varphi_1\right) + c_{dfr}\left(\dot{z} - \dot{\theta}_s l_f - e_{u1}\dot{\varphi}_s - \dot{z}_1 + e_{u1}\dot{\varphi}_1\right) \tag{16}$$

$$F_{srl} = k_{srl}(z_F - z_{F'}) + c_{drl}\left(\dot{z}_E - \dot{z}_{E'}\right) = k_{srl}(z + \theta_s l_r + e_{u2}\varphi_s - z_2 - e_{u2}\varphi_2) + c_{drl}\left(\dot{z} + \dot{\theta}_s l_r + e_{u2}\dot{\varphi}_s - \dot{z}_2 - e_{u2}\dot{\varphi}_2\right) \tag{17}$$

$$F_{srr} = k_{srr}(z_E - z_{E'}) + c_{drr}\left(\dot{z}_E - \dot{z}_{E'}\right) = k_{srr}(z + \theta_s l_r - e_{u2}\varphi_s - z_2 + e_{u2}\varphi_2) + c_{drr}\left(\dot{z} + \dot{\theta}_s l_r - e_{u2}\dot{\varphi}_s - \dot{z}_2 + e_{u2}\dot{\varphi}_2\right) \tag{18}$$

The bus body vertical motion is described by Eqs.(19) and (20)

$$m_s \ddot{z} = F_d + F_{p1} + F_{p2} + F_{p3} - F_{sfl} - F_{sfr} - F_{srl} - F_{srr} + F_{zwind,v} \tag{19}$$

$$\begin{aligned} m_s \ddot{z} = &-\left(c_{df_{eq}} + c_{dr_{eq}} + c_d + c_{p1} + c_{p2} + c_{p3}\right)\dot{z} - \left(k_{sf_{eq}} + k_{sr_{eq}} + k_d + k_{p1} + k_{p2} + k_{p3}\right)z - \left(c_d s_1 - c_{p1} s_3 - c_{p2} s_5 + c_{p3} s_7\right)\dot{\varphi}_s \\ &- \left(k_d s_1 - k_{p1} s_3 - k_{p2} s_5 + k_{p3} s_7\right)\varphi_s + \left(c_d s_2 + c_{p1} s_4 - c_{p2} s_6 - c_{p3} s_8 + 2 l_f c_{df_{eq}} - 2 l_r c_{dr_{eq}}\right)\dot{\theta}_s + \left(k_d s_2 + k_{p1} s_4 - k_{p2} s_6 + k_{p3} s_8 \right. \\ &\left. + 2 l_f k_{sf_{eq}} - 2 l_r k_{sr_{eq}}\right)\theta_s + c_d \dot{z}_d + k_d z_d + c_{p1}\dot{z}_{p1} + k_{p1} z_{p1} + c_{p2}\dot{z}_{p2} + k_{p2} z_{p2} + c_{p3}\dot{z}_{p3} + k_{p3} z_{p3} + c_{df_{eq}}\dot{z}_1 + k_{sf_{eq}} z_1 + c_{dr_{eq}}\dot{z}_2 + k_{sr_{eq}} z_2 \\ &+ F_{zwind,v} \end{aligned} \tag{20}$$

The bus front axle motion in the vertical direction is given by Eqs.(21) and (22)

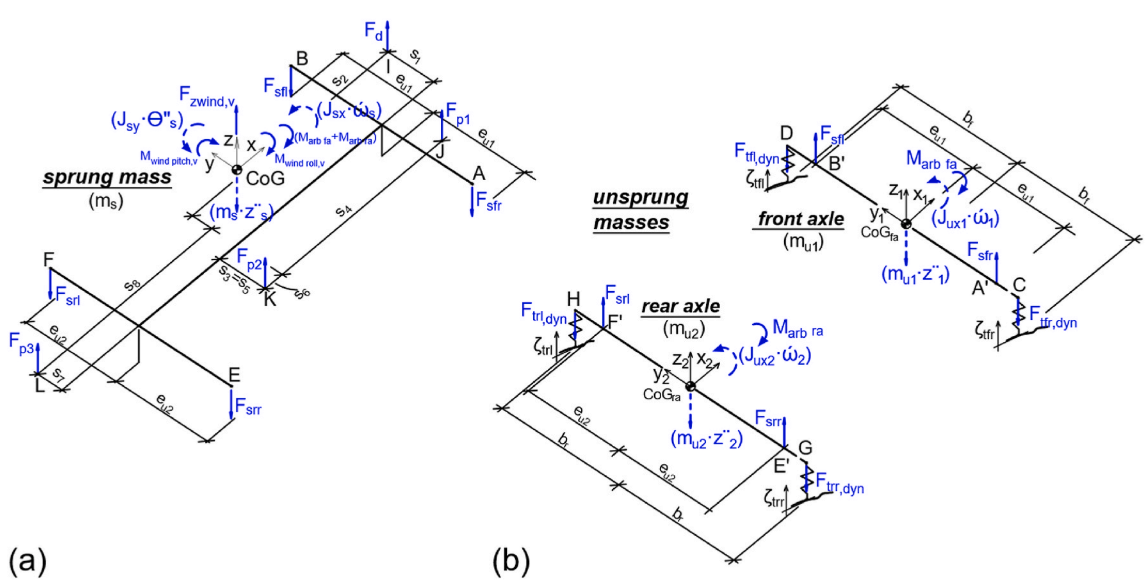

Fig. 5. FBDs of bus a) sprung mas; b) unsprung masses.

$$m_{u1}\ddot{z}_1 = F_{sfl} + F_{sfr} - F_{tfl,dyn} - F_{tfr,dyn} \tag{21}$$

$$\begin{aligned} m_{u1}\ddot{z}_1 = & -2c_{dfl}\dot{z}_1 - 2\left(k_{sfl}+k_{tfl}\right)z_1 + 2c_{dfl}\dot{z} + 2k_{sfl}z - 2c_{dfl}l_f\dot{\theta}_s \\ & -2k_{sfl}l_f\theta_s + k_{tfr}\zeta_{tfr} + k_{tfl}\zeta_{tfl} \end{aligned} \tag{22}$$

where $F_{tfl,\ dyn}$ and $F_{tfr,\ dyn}$ are dynamic front tyre forces given by Eqs.(10) and (11) in (Sekulic et al., 2021).

The bus rear axle motion in the vertical direction is given by Eqs.(23) and (24)

$$m_{u2}\ddot{z}_2 = F_{srl} + F_{srr} - F_{trl,dyn} - F_{trr,dyn} \tag{23}$$

$$\begin{aligned} m_{u2}\ddot{z}_2 = & -2c_{drl}\dot{z}_2 - 2(k_{srl}+k_{trl})z_2 + 2c_{drl}\dot{z} + 2k_{srl}z - 2c_{drl}l_r\dot{\theta}_s \\ & -2k_{srl}l_r\theta_s + k_{trr}\zeta_{trr} + k_{trl}\zeta_{trl} \end{aligned} \tag{24}$$

where $F_{trl,\ dyn}$ and $F_{trr,\ dyn}$ are dynamic rear tyre forces given by Eqs.(14) and (15) in (Sekulic et al., 2021).

The pitch motion of the bus sprung mass, according to Fig. 5a, is shown by Eqs.(25) and (26)

$$\begin{aligned} J_{sy}\ddot{\theta}_s = & -F_d s_2 - F_{p1}s_4 + \left(F_{sfl}+F_{sfr}\right)l_f - \left(F_{srl}+F_{srr}\right)l_r \\ & + F_{p2}s_6 + F_{p3}s_8 + M_{wind\ pitch,v} \end{aligned} \tag{25}$$

$$\begin{aligned} J_{sy}\ddot{\theta}_s = & -\left(s_2^2c_d + s_4^2c_{p1} + s_6^2c_{p2} + s_8^2c_{p3} + 2c_{dfr}l_f^2 + 2c_{drr}l_r^2\right)\dot{\theta}_s \\ & -\left(s_2^2k_d + s_4^2k_{p1} + s_6^2k_{p2} + s_8^2k_{p3} + 2k_{sfr}l_f^2 + 2k_{srr}l_r^2\right)\theta_s \\ & - s_2c_d\dot{z}_d - s_2k_dz_d - s_4c_{p1}\dot{z}_{p1} - s_4k_{p1}z_{p1} + s_6c_{p2}\dot{z}_{p2} + s_6k_{p2}z_{p2} \\ & + s_8\ c_{p3}\dot{z}_{p3} + s_8\ k_{p3}z_{p3} + \left(s_2c_d + s_4c_{p1} - s_6c_{p2} - s_8c_{p3} + 2l_fc_{dfr}\right. \\ & \left. - 2l_rc_{drr}\right)\dot{z} + \left(s_2k_d + s_4k_{p1} - s_6k_{p2} - s_8k_{p3} + 2l_fk_{sfr} - 2l_rk_{srr}\right)z \\ & + \left(s_1s_2c_d - s_3s_4c_{p1} + s_5s_6c_{p2} - s_7s_8c_{p3}\right)\dot{\varphi}_s + \left(s_1s_2k_d - s_3s_4k_{p1}\right. \\ & \left. + s_5s_6k_{p2} - s_7s_8k_{p3}\right)\varphi_s - 2l_fc_{dfr}\dot{z}_1 - 2l_fk_{sfr}z_1 + 2l_rc_{drr}\dot{z}_2 \\ & + 2l_rk_{srr}z_2 + M_{wind\ pitch,v} \end{aligned} \tag{26}$$

Fig. 6 presents FBDs of the coach sprung and unsprung masses with active forces, active moments and fictive moment acting on them. These are used for the definition of EOMs for roll motions of the bus body, as well as the front and rear axles.

Roll equilibrium for the coach sprung mass is given by Eqs.(27) and (28)

$$\begin{aligned} J_{sx}\dot{\omega}_s = & \left(m_sg - F_{z\ wind,v}\right)\Delta h_{sm}\varphi_s + m_sa_y\Delta h_{sm} + \left(F_{sfr} - F_{sfl}\right)e_{u1} \\ & + \left(F_{srr} - F_{srl}\right)e_{u2} - \left(M_{arb,fa} + M_{arb,ra}\right) - F_{p1}s_3 - F_{p2}s_5 \\ & + F_{p3}s_7 + F_ds_1 + M_{wind_{roll},v} \end{aligned} \tag{27}$$

$$\begin{aligned} J_{sx}\dot{\omega}_s = & \left(m_sg - F_{z\ wind,v}\right)\Delta h_{sm}\varphi_s + m_sa_y\Delta h_{sm} - \left(s_1^2c_d + s_3^2c_{p1} + s_5^2c_{p2} + s_7^2c_{p3}\right. \\ & \left. + 2c_{dfr}e_{u1} + 2c_{drr}e_{u2}\right)\dot{\varphi}_s - \left(s_1^2k_d + s_3^2k_{p1} + s_5^2k_{p2} + s_7^2k_{p3}\right. \\ & \left. + 2k_{sfr}e_{u1} + 2k_{srr}e_{u2} + K_{arb_f} + K_{arb_r}\right)\varphi_s + \left(s_1s_2c_d - s_3s_4c_{p1}\right. \\ & \left. + s_5s_6c_{p2} - s_7s_8c_{p3}\right)\dot{\theta}_s + \left(s_1s_2k_d - s_3s_4k_{p1} + s_5s_6k_{p2}\right. \\ & \left. - s_7s_8k_{p3}\right)\theta_s - \left(s_1c_d - s_3c_{p1} - s_5c_{p2} + s_7c_{p3}\right)\dot{z} - \left(s_1k_d - s_3k_{p1}\right. \\ & \left. - s_5k_{p2} + s_7k_{p3}\right)z + 2c_{dfr}e_{u1}^2\dot{\varphi}_1 + \left(2k_{sfr}e_{u1}^2 + K_{arb_f}\right)\varphi_1 \\ & + 2c_{drr}e_{u2}^2\dot{\varphi}_2 + \left(2k_{srr}e_{u2}^2 + K_{arb_r}\right)\varphi_2 + s_1c_d\dot{z}_d + s_1k_dz_d \\ & - s_3c_{p1}\dot{z}_{p1} - s_3k_{p1}z_{p1} - s_5c_{p2}\dot{z}_{p2} - s_5k_{p2}z_{p2} + s_7c_{p3}\dot{z}_{p3} \\ & + s_7k_{p3}z_{p3} + M_{wind_{roll},v} \end{aligned} \tag{28}$$

Roll equilibrium for the front/rear axle takes the same final forms as in (Sekulic et al., 2021), and is given by Eq. (29) and Eq. (30).

$$\begin{aligned} J_{ux1}\dot{\omega}_1 = & K_{\varphi f}(\varphi_s - \varphi_1) + C_{\varphi f}(\omega_s - \omega_1) + \left(F_{yfl} + F_{yfr}\right)\cos\,\delta h_{RCfa} \\ & + \left(z_1 - \varphi_1b_f - \zeta_{tfr}\right)k_{tfr}b_f - \left(z_1 + \varphi_1b_f - \zeta_{tfl}\right)k_{tfl}b_f \\ & + K_{arb_f}(\varphi_s - \varphi_1) \end{aligned} \tag{29}$$

$$\begin{aligned} J_{ux2}\dot{\omega}_2 = & K_{\varphi r}(\varphi_s - \varphi_2) + C_{\varphi r}(\omega_s - \omega_2) + \left(F_{yrl} + F_{yrr}\right)h_{RCra} \\ & + \left(z_2 - \varphi_2b_r - \zeta_{trr}\right)k_{trr}b_r - \left(z_2 + \varphi_2b_r - \zeta_{trl}\right)k_{trl}b_r + K_{arb_r}(\varphi_s - \varphi_2) \end{aligned} \tag{30}$$

where $K_{\varphi f}$, $K_{\varphi r}$, are roll stiffness for the bus front and rear axles; $C_{\varphi f}$, $C_{\varphi r}$ are roll damping for the bus front and rear axles; K_{arbf}, K_{arbr} are anti-roll bar stiffness for the bus front and rear axles (Table 3). Roll stiffness and roll damping are given by Eqs.(31) and (32)

$$K_{\varphi f} = \frac{1}{2}k_{sfl}(2e_{u1})^2\ ;\ K_{\varphi r} = \frac{1}{2}k_{sfr}(2e_{u2})^2 \tag{31}$$

$$C_{\varphi f} = \frac{1}{2}c_{sfl}(2e_{u1})^2\ ;\ C_{\varphi r} = \frac{1}{2}c_{sfr}(2e_{u2})^2 \tag{32}$$

2.2. Calculation of the lateral accelerations acting on bus users' bodies

Fig. 7a shows the bus sprung mass with positions of three receiving points (floor, seat surface, and backrest, see Fig. 15) for the driver and passengers. Lateral accelerations acting on the driver and passenger1 from their seats due to bus body roll motion are calculated by Eqs.(33) and (34) based on Fig. 7b.

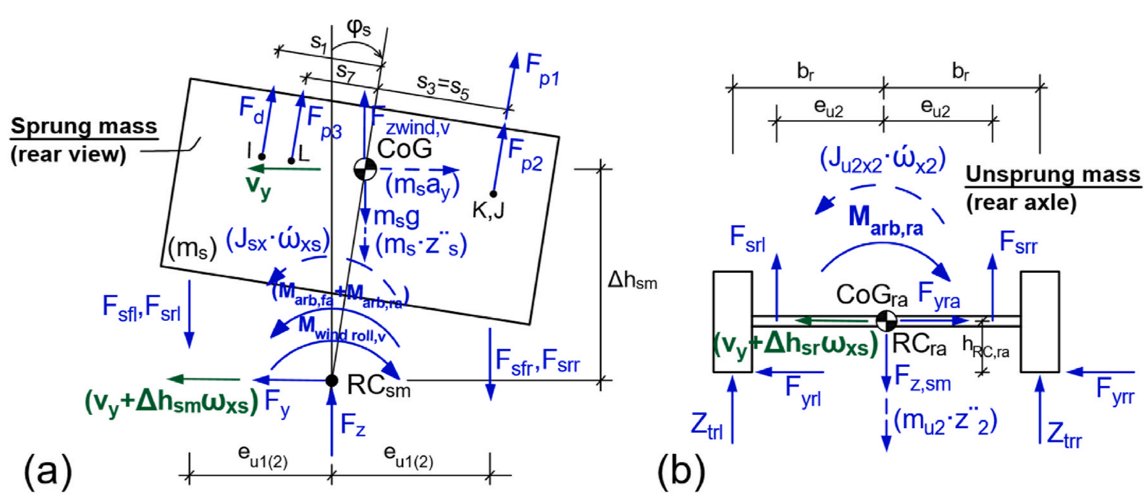

Fig. 6. FBDs of the bus a) sprung mass; b) unsprung mass for definition of roll dynamics.

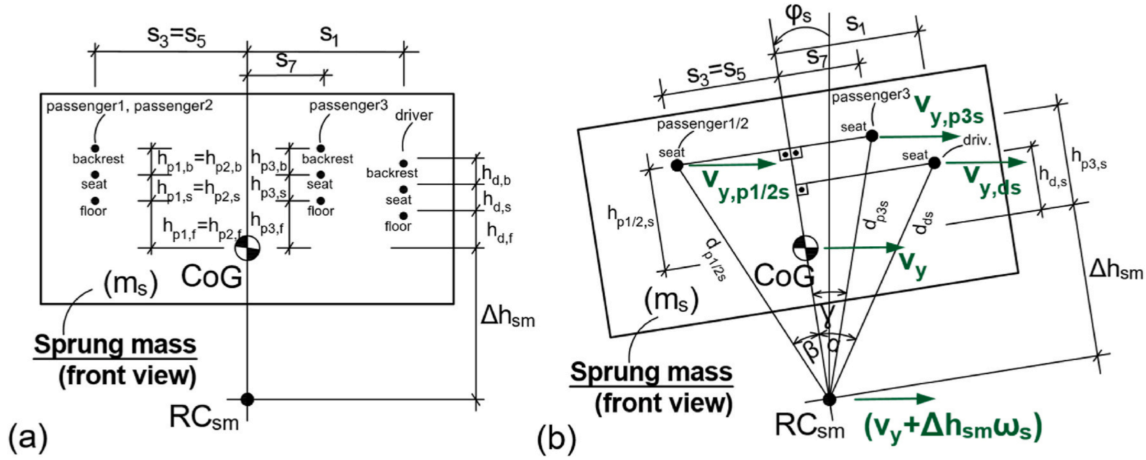

Fig. 7. Bus users' receiving points a) position; b) lateral velocity at the users' seats.

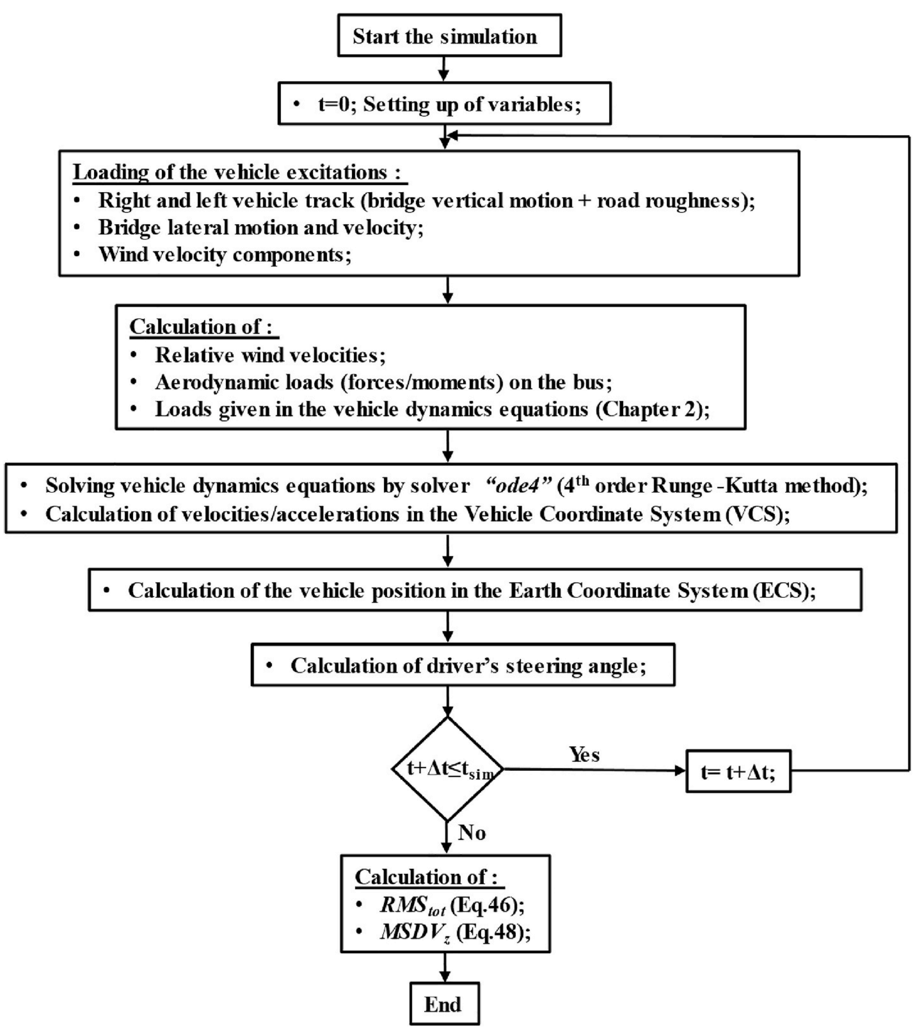

Fig. 8. Flowchart for bus users' ride comfort and motion sickness analysis.

$$\dot{v}_{y,ds} = \left(\dot{v}_y + \Delta h_{sm}\dot{\omega}_s\right) - d_{ds}\dot{\omega}_s \cdot \cos\alpha = \dot{v}_y - \left(\sqrt{\left(\Delta h_{sm} + h_{d,s}\right)^2 + s_1^2} \cdot \cos\alpha - \Delta h_{sm}\right)\dot{\omega}_s \tag{33}$$

$$\dot{v}_{y,p1s} = \left(\dot{v}_y + \Delta h_{sm}\dot{\omega}_s\right) - d_{p1s}\dot{\omega}_s \cdot \cos\beta = \dot{v}_y - \left(\sqrt{\left(\Delta h_{sm} + h_{p1,s}\right)^2 + s_3^2} \cdot \cos\beta - \Delta h_{sm}\right)\dot{\omega}_s \tag{34}$$

where $h_{d,f}$, $h_{d,s}$ and $h_{d,b}$ are heights of the driver receiving points (floor, seat and backrest) with respect to bus CoG (Table 3); $h_{p1,f}$, $h_{p1,s}$ and $h_{p1,b}$ are heights of the passenger1 receiving points (floor, seat and backrest) with respect to bus CoG (Table 3).

Similarly, lateral accelerations acting on passenger2 and passenger3 from their seats due to bus body roll motion are given by Eqs.(35) and (36)

$$\dot{v}_{y,p2s} = \dot{v}_y - \left(\sqrt{\left(\Delta h_{sm} + h_{p2,s}\right)^2 + s_5^2} \cdot \cos\beta - \Delta h_{sm}\right)\dot{\omega}_s \tag{35}$$

$$\dot{v}_{y,p3s} = \dot{v}_y - \left(\sqrt{\left(\Delta h_{sm} + h_{p3,s}\right)^2 + s_7^2} \cdot \cos\gamma - \Delta h_{sm}\right)\dot{\omega}_s \tag{36}$$

where $h_{p2,f}$, $h_{p2,s}$ and $h_{p2,b}$ are heights of the passenger2 receiving points (floor, seat and backrest) with respect to bus CoG (Table 3); $h_{p3,f}$, $h_{p3,s}$ and $h_{p3,b}$ are heights of the passenger3 receiving points (floor, seat and backrest) with respect to bus CoG (Table 3).

When considering bus yaw motion (Figs. 2a and 3), total lateral accelerations at bus users' seats are given by Eqs.(37)-(40)

$$\dot{v}_{y,driver\_seat} = \dot{v}_{y,ds} + \sqrt{s_1^2 + s_2^2} \cdot \dot{\omega}_z \tag{37}$$

$$\dot{v}_{y,passenger1\_seat} = \dot{v}_{y,p1s} + \sqrt{s_3^2 + s_4^2} \cdot \dot{\omega}_z \tag{38}$$

$$\dot{v}_{y,passenger2\_seat} = \dot{v}_{y,p2s} - \sqrt{s_5^2 + s_6^2} \cdot \dot{\omega}_z \tag{39}$$

$$\dot{v}_{y,passenger3\_seat} = \dot{v}_{y,p3s} - \sqrt{s_7^2 + s_8^2} \cdot \dot{\omega}_z \tag{40}$$

Lateral accelerations from the bus floor acting on the users' feet and backrest acting on the users' back are calculated in a similar way as explained above based on Fig. 7.

2.3. Brief description of the bus driver model

A pure pursuit driver model was presented in (Sekulic et al., 2021). This driver model works together with a coach model when running across the floating bridge. Experimental studies were carried out on the CASTER driving simulator to adjust the driver model's parameters (e.g. look-ahead time). A thorough description of the driver model can be found in (Sekulic et al., 2021).

2.4. Overall simulation process in ride comfort and motion sickness analysis

Flowchart of the overall simulation process is presented in Fig. 8. Solver ***ode 4*** (4th order Runge-Kutta method), with fixed-size time step of $\Delta t = 0.001\ s$, is used when solving non-linear vehicle dynamics equations. Simulation time (t_{sim}) in our investigation is equal to the vehicle traveling time over the floating bridge. For example, simulation time for the vehicle speed at 36 km/h is 524 s.

3. Vehicle model excitations

The floating bridge will be located on Bjørnafjorden, connecting areas around Bergen and Stavanger (Fig. 1a). It is an open area to the North Sea, therefore it is exposed to strong winds and waves during harsh weather conditions. These perturbances will cause bridge deck displacements with vertical (z_{br}), lateral (y_{br}) and roll (φ_{br}) motions as dominant ones (Fig. 9a). Floating bridge motions and wind loads on a coach will influence vehicle and driver behaviour when running across the bridge (Sekulic et al., 2021). Bridge motion intensities depend on wind and wave intensities, i.e. storm conditions severity (Sekulic et al., 2023).

3.1. Definition of storm conditions

The definitions of the storm conditions (W1-W10) are given in Table 1. Each storm condition is described by waves, swells and wind characteristics (Table 1). Waves are generated locally at the site of the floating bridge by the wind (i.e. from the friction of the sea surface and the wind) and are short periodic waves. Swells are waves that have travelled over the ocean and reach Bjørnafjorden from the North Sea. These waves are long periodic waves generated from storms far from the floating bridge location. The overall wave conditions (both wind-generated and swells) at the surface elevation of the bridge are simulated by superimposing waves generated from two Jonswap spectra (Vegvesen, 2017). A Kaimal wind spectrum was used to create a wind field (Branlard, 2010) with mean wind speed w_s (Table 1) and the turbulence characteristic I_u, as shown in Eq. (41).

$$I_u = \frac{1}{ln\left(\frac{z}{0.01}\right)} \tag{41}$$

where z is the height [m].

For 1-year storm condition a wind field was generated from a Kaimal wind spectrum with mean wind speed $w_s = 21.40$ m/s and along turbulence $I_u = 0.15$. The structure was excited by waves generated from a Jonswap spectrum with significant wave height ($H_s = 1.2$ m) and peak

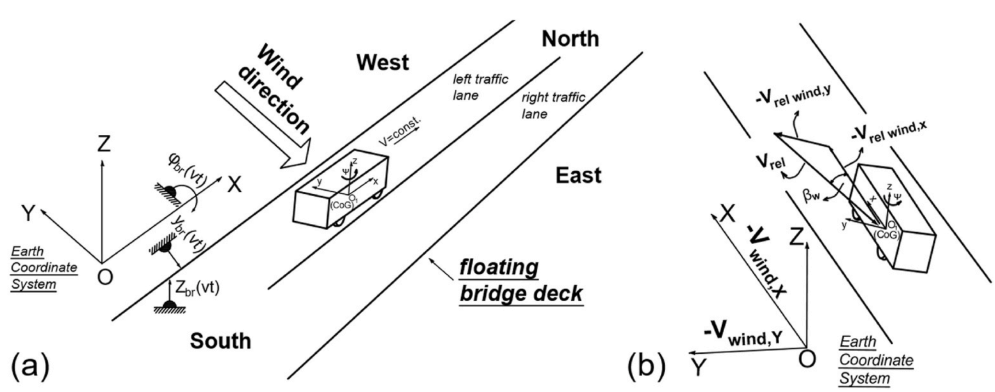

Fig. 9. Excitations a) floating bridge deck motions; b) components of the wind velocity.

Table 1
Ten storm conditions (W1-W10).

Storm condition	Waves			Swell			Wind - [1hr - 10m]	
	Dir [°]	Hs [m]	Tp [s]	Dir [°]	Hs [m]	Tp [s]	Dir [°]	ws [m/s]
W1 (< 1-year storm)	315.00	0.20	2.07	300.00	0.04	17.00	315.00	6.13
W2 (< 1-year storm)	315.00	0.40	2.73	300.00	0.07	17.00	315.00	9.84
W3 (< 1-year storm)	315.00	0.60	3.22	300.00	0.11	17.00	315.00	13.08
W4 (< 1-year storm)	315.00	0.80	3.61	300.00	0.15	17.00	315.00	15.99
W5 (< 1-year storm)	315.00	1.00	3.96	300.00	0.18	17.00	315.00	18.73
W6 (1-year storm)	315.00	1.20	4.26	300.00	0.22	17.00	315.00	21.40
W7 (2-year storm)	315.00	1.40	4.53	300.00	0.25	17.00	315.00	23.60
W8 (10-year storm)	315.00	1.60	4.78	300.00	0.28	17.00	315.00	25.80
W9 (50-year storm)	315.00	1.80	5.02	300.00	0.33	17.00	315.00	28.50
W10 (100-year storm)	315.00	2.00	5.24	300.00	0.34	17.00	315.00	29.60

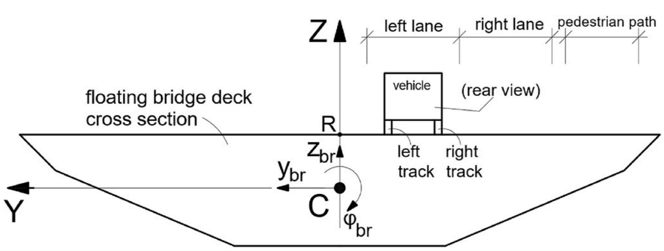

Fig. 10. Floating bridge cross-section with characteristic points and dominant motions.

period ($T_p = 4.26$ s). Small swell waves propagating into the fjord from the North-Sea were also considered ($H_s = 0.22$ m, $T_p = 17$ s) (Vegvesen, 2017).

3.2. Floating bridge excitations

Bjørnafjorden floating bridge is part of the coastal highway route E39 Norway's road project, and currently it is in its design phase. Bridge deck motions were simulated in *Orcaflex* software. Simulation of bridge motions under the influence of environmental loads (wind and waves) was performed for 1 h (3600 s) of simulation time. Bridge deck motions (point C, Fig. 10) depend on two values - vehicle position on the deck and on time. Consequently, vehicle excitations will not be the same for different vehicle speed. Detailed working procedure on data for obtaining vehicle inputs for numerical simulations could be found in (Sekulic et al., 2021).

Fig. 11 shows vertical bridge deck motion for three different storm conditions (W5, W6 and W7). Vertical bridge deck motion includes roughness of A/B road class modelled by standard ISO 8608 (Sekulic et al., 2021; Rana and Asaduzzaman, 2021). It could be noticed that the intensity of the bridge motion increases with the severity of the storm. These vertical bridge deck motions were used to define the left and right vehicle track excitations (Sekulic et al., 2021).

Fig. 12 shows lateral bridge deck motions for three storm conditions. It could be noticed that lateral bridge motion increases with storm severity. These motions are used to define the path the vehicle needs to follow and for the driver model inputs (Sekulic et al., 2021). Fig. 13 shows lateral bridge velocities for three different storms. It could be seen that lateral velocities increase with the storm intensity. These excitations are used for bus lateral tyre forces calculation (Sekulic et al., 2021).

Fig. 14 shows the bridge deck's roll motions for three storm conditions. Roll motion angles increase with storm severity. For example, for W5, roll angle values are in the range of ±0.2°, whereas for W7, they are in the range of ±0.4°. These values, together with the bridge deck's vertical motions, are used to define the left and right excitation inputs for the bus model (Sekulic et al., 2021).

3.3. Wind excitations on vehicle model

Wind velocity data are simulated in *WindSim* software (Vegvesen, 2017; Sekulic et al., 2021). Turbulent wind time series are simulated in the *WindSim* code for a set of positions based on mean wind speed, single point gust spectrum and coherence functions. The code is using inverse

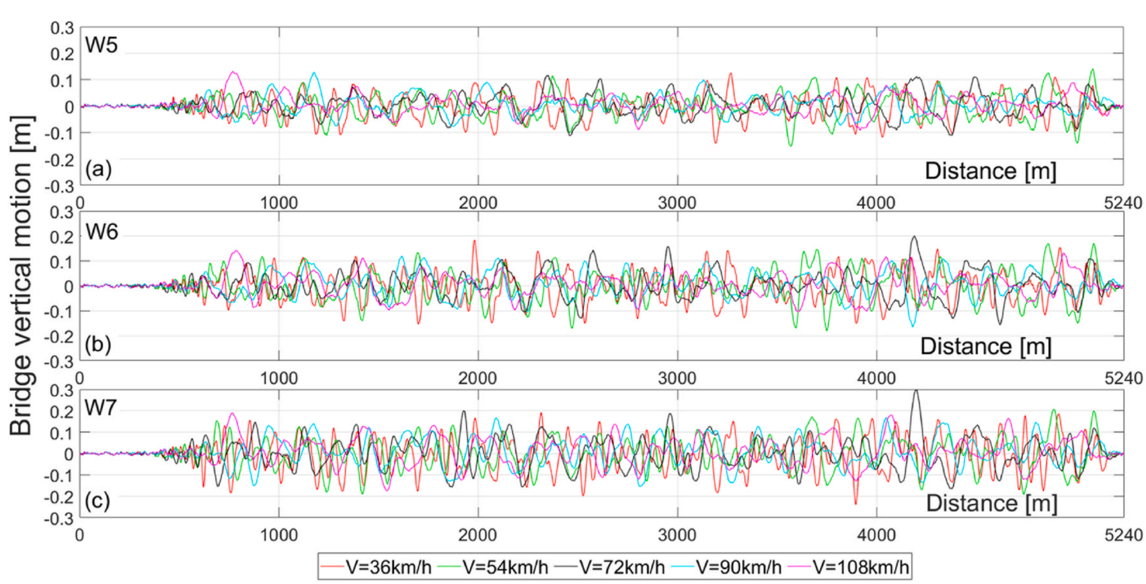

Fig. 11. Bridge vertical motion for storm a) W5; b) W6; c) W7 as a function of vehicle velocity.

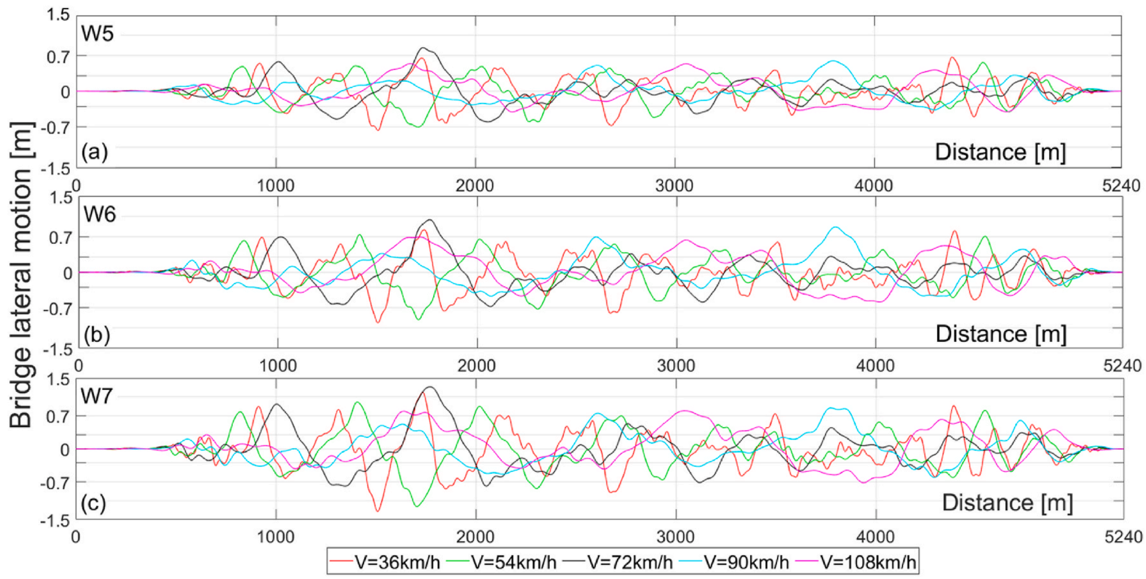

Fig. 12. Bridge lateral motion for storm a) W5. b) W6; c) W7 as a function of vehicle velocity.

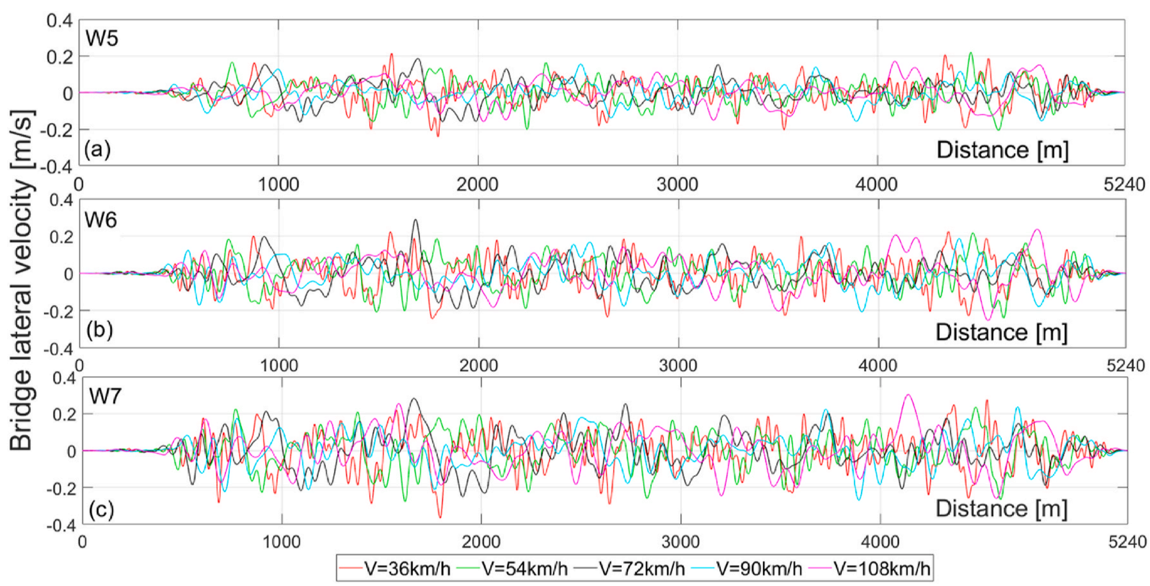

Fig. 13. Bridge lateral velocity for storm a) W5; b) W6; c) W7 as a function of vehicle speed.

FFT (the fast Fourier transform) to generate the wind speed time series from a spectral description of the fluctuating wind components.

The mean wind speed is defined in the design basis as the 1-h average at 10 m above sea level. The vertical wind profile is described by Eq. (42).

$$U(z) = U_{10} \cdot \left(\frac{z}{10}\right)^{\alpha} \tag{42}$$

where U_{10} is the mean wind speed at 10 m height; α is the profile factor of the wind profile (α is defined as 0.127 in the metocean report (Vegvesen, 2017)). The fluctuating wind spectrum is defined according to Eurocode NS-EN 1991-1-4:2005/NS 3491–4:2002 and N400 (Vegvesen, 2017).

The turbulence spectrum as function of frequency n and integral length scale L_i is defined by Eq. (43) (according to N400 (Vegvesen and N400 Bruprosjektering, 2015) for wind components $i = u,v,w$, (u - longitudinal; v - transversal; w - vertical)):

$$\frac{nS_i}{\sigma_i^2} = \frac{A_i \widehat{n}_i}{\left(1 + 1.5A_i \widehat{n}_{ii}\right)^{5/3}} \tag{43}$$

where A_i is integral length scale factors ($A_u = 6.48$; $A_v = A_w = 9.4$); $\widehat{n}_i$ – is frequency given by Eq. (44).

$$\widehat{n}_i = \frac{nL_i(z)}{U(z)} \tag{44}$$

where $L_i(z)$ is integral length scale. The integral length scale is 132 m calculated in accordance with N400 (Vegvesen and N400 Bruprosjektering, 2015) at the reference height.

The coherence function is an exponential decay function defined by Eq. (45)

$$\sqrt{coh(n\Delta S)} = exp\left(-C_i \frac{n\Delta S}{U(z)}\right) \tag{45}$$

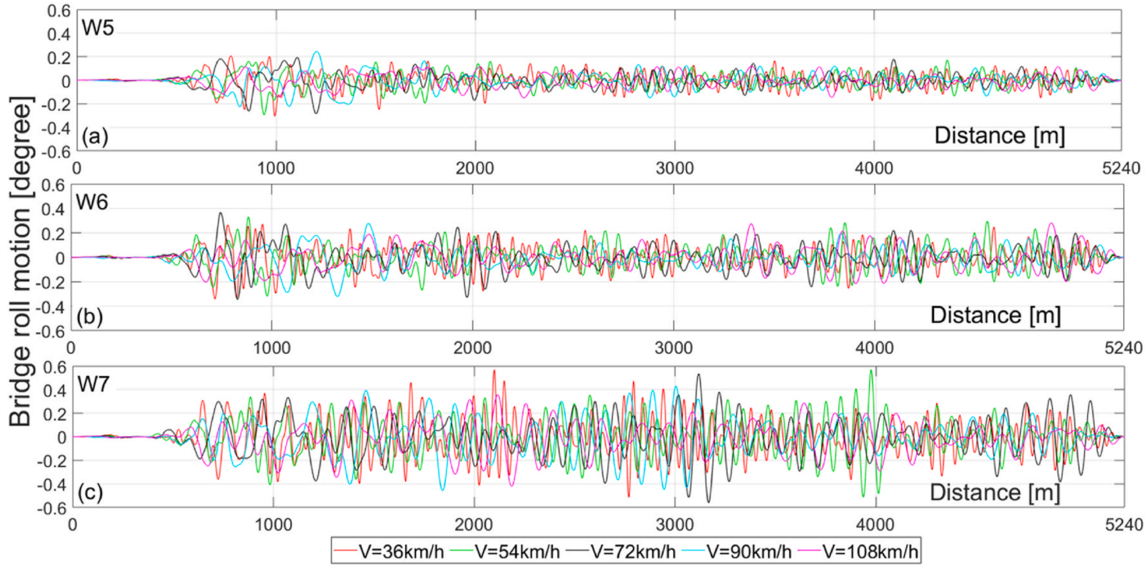

Fig. 14. Bridge roll motion for storm a) W5; b) W6; c) W7 as a function of vehicle speed.

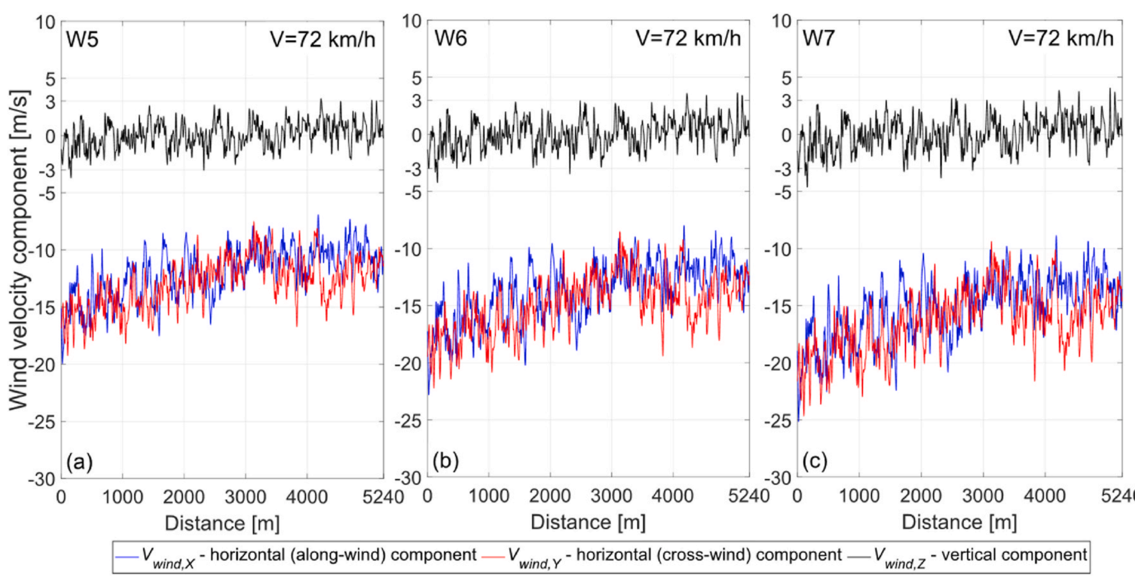

Fig. 15. Components of the wind velocity for a) W5; b) W6; c) W7 weather condition and for the vehicle velocity of 72 km/h.

where C_i is the decay factor for each wind component ($C_u = 10$; $C_v = C_w = 6.5$).

The simulated wind signal was quite stochastic in nature, covering both changing directions and magnitudes of the instantaneous wind velocities. This signal was later used to generate aerodynamic forces that ended up having a similar stochastic behaviour. This is not an ideal representation of the stormy wind conditions, but any other approaches were considered to be significantly more computationally expensive.

A detailed data preparation procedure for coach wind load inputs is explained in (Sekulic et al., 2021). As an example, Fig. 15 shows wind velocity components for three storm conditions for vehicle velocity of 72 km/h, which is defined in the ECS (Fig. 9b). It could be noticed that the magnitudes of the along-wind and cross-wind components increase with the severity of the storm. Horizontal wind components were transformed from ECS to VCS and used for relative wind velocity calculations (Fig. 9b). Relative wind velocities served for calculations of aerodynamic forces/moments acting on the bus (Sekulic et al., 2021). The vertical wind component values are small (in the range ±3 m/s, Fig. 15) and considered minor compared to horizontal components. Hence, vertical wind components were not taken in aerodynamic load calculations (Sekulic et al., 2021).

4. Method for ride comfort and motion sickness assessment - ISO 2631/1997

Standard ISO 2631/1997 proposes a method for analysing vibrational influence on a human body with respect to motion sickness, comfort, perception, and health (ISO 2631, 1997). The method considers different body positions (standing, seated, and recumbent) and different receiving points (e.g. feet, seat surface, back, etc.).

Fig. 16 shows a bus user in a seated position and appropriate receiving points with their axles. Bus driver and passengers are exposed to translational and angular vibration acting on their feet from the bus floor, on their buttocks from their seats and on their backs from their seat backrests. The comfort analysis does not consider vibration acting on a driver's hand from the bus steering wheel.

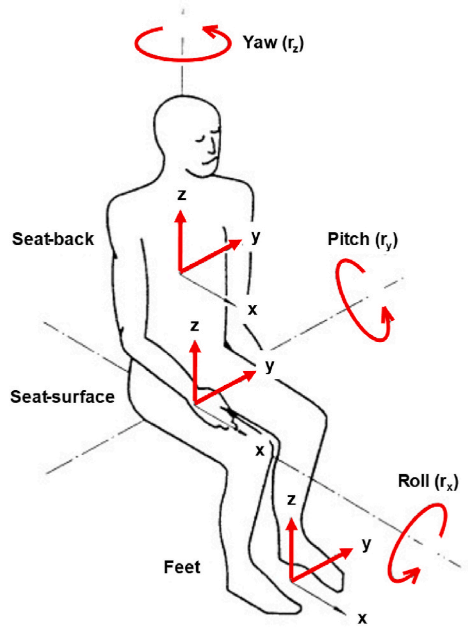

Fig. 16. Bus user body in a seated position and receiving points with their axles.

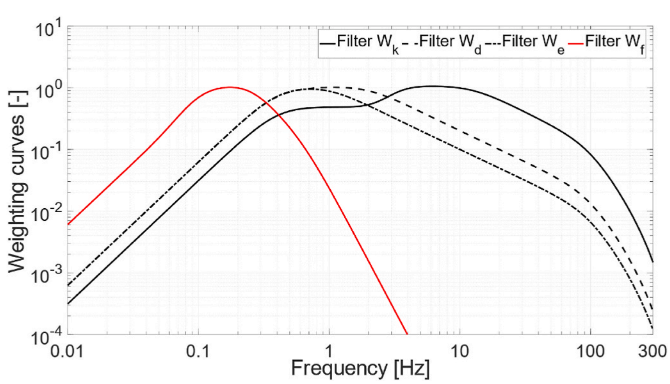

Fig. 17. Frequency-weighting curves for ride comfort and motion sickness assessment.

4.1. Ride comfort

ISO 2631 suggests total Root-Mean-Square (*RMS*) value and criteria for ride comfort assessment in means of public transport for ride comfort assessment (ISO 2631, 1997). In this work, the total *RMS* value is calculated considering translational and rotational vibration from three receiving points (marked with red lines in Fig. 16). The total *RMS* value is calculated by Eq. (46)

Table 2
Ride comfort ISO 2631/1997 criteria.

Vibration intensity [m/s^2]	Comfort assessment
<0.315	comfortable
0.315–0.63	a little uncomfortable
0.5–1.0	fairly uncomfortable
0.8–1.6	uncomfortable
1.25–2.5	very uncomfortable
>2.0	extremely uncomfortable

$$RMS_{tot} = \Bigg(\left(k_{z,floor}\cdot\ddot{z}_{w,RMS\_floor}\right)^2 + \left(k_{y,floor}\cdot\ddot{y}_{w,RMS\_floor}\right)^2 + \left(k_{z,seat}\cdot\ddot{z}_{w,RMS\_seat}\right)^2 + \left(k_{y,seat}\cdot\ddot{y}_{w,RMS\_seat}\right)^2 + \left(k_{roll,seat}\cdot\ddot{\varphi}_{w,RMS\_seat}\right)^2 + \left(k_{pitch,seat}\cdot\ddot{\theta}_{w,RMS\_seat}\right)^2 + \left(k_{yaw,seat}\cdot\ddot{\psi}_{w,RMS\_seat}\right)^2 + \left(k_{z,seat-back}\cdot\ddot{z}_{w,RMS\_seat-back}\right)^2 + \left(k_{y,seat-back}\cdot\ddot{y}_{w,RMS\_seat-back}\right)^2\Bigg)^{\frac{1}{2}} \tag{46}$$

where $k_{z,floor}$, $k_{y,floor}$, $k_{z,seat}$, $k_{y,seat}$, $k_{roll,\ seat}$, $k_{pitch,\ seat}$, $k_{yaw,\ seat}$, $k_{z,seat\text{-}back}$, $k_{y,seat\text{-}back}$ are multiplying factors whose values depend on receiving points and axles (Table 5); $\ddot{z}_{w,RMS\_floor}$, $\ddot{y}_{w,RMS\_floor}$, $\ddot{z}_{w,RMS\_seat}$, $\ddot{y}_{w,RMS\_seat}$, $\ddot{\varphi}_{w,RMS\_seat}$, $\ddot{\theta}_{w,RMS\_seat}$, $\ddot{\Psi}_{w,RMS\_seat}$, $\ddot{z}_{w,RMS\_seat\text{-}back}$, $\ddot{y}_{w,RMS\_seat\text{-}back}$ are *RMS* values of frequency weighted accelerations for considered receiving points and their axles.

For instance, the *RMS* value of frequency-weighted acceleration from a user's seat is given by Eq. (47)

$$\ddot{z}_{w,RMS\_seat} = \sqrt{\frac{1}{T}\int_0^T \left(\ddot{z}_{w,seat}(t)\right)^2 dt} \tag{47}$$

where $\ddot{z}_w(t)$ is frequency-weighted vertical acceleration. Fig. 17 shows three frequency-weighting curves used for acceleration filtering (W_k - for acceleration along the *z-axis* at seat and feet, and the *y-axis* at feet; W_d - for acceleration along the *y-axis* at seat and seat-back and along the *z-axis* at seat-back; W_e - for rotational (roll, pitch, yaw) acceleration at seat).

As an example, Fig. 18a shows raw and weighted vertical accelerations at the driver's seat in the time domain for coach velocity of 72 km/h. It could be noticed that the weighted acceleration is of lower values than the raw acceleration (Fig. 18c). Fig. 18b shows raw and weighted vertical accelerations in the frequency domain. Acceleration intensity below 0.5 Hz is not considered in the evaluation of driving comfort, according to (ISO 2631, 1997).

Table 2 presents the criteria for ride comfort assessment in public transport (ISO 2631, 1997).

4.2. Motion sickness

ISO 2631 suggests motion sickness dose value (*MSDVz*) for motion sickness assessment. Higher *MSDVz* values correspond to a greater incidence of motion sickness (ISO 2631, 1997). *MSDVz* considers vibration at the seat in the vertical direction only and is given by Eq. (48)

$$MSDV_z = \sqrt{\int_0^T \left(\ddot{z}_{w,seat}(t)\right)^2 dt} \tag{48}$$

where $\ddot{z}_{w,seat}$ is the frequency-weighted acceleration in the vertical direction from users' seats; T is the vibration time of the exposure. The frequency-weighting curve (W_f) used for vertical acceleration filtering is presented in Fig. 17.

As an example, Fig. 19a shows raw and weighted vertical accelerations at the driver's seat in the time domain for bus speed of 36 km/h. Fig. 19b shows raw and weighted vertical accelerations in the frequency domain. Acceleration intensity in the frequency range of 0.1–0.5 Hz is only considered in the evaluation of motion sickness, according to (ISO 2631, 1997).

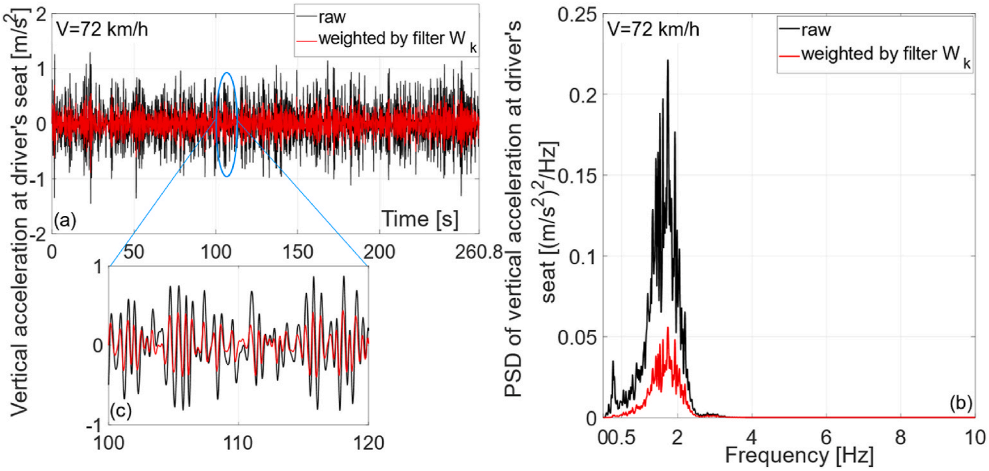

Fig. 18. Raw and weighted vertical acceleration at driver seat surface a) in the time domain; b) in the frequency domain; c) magnified view, for a vehicle velocity of 72 km/h.

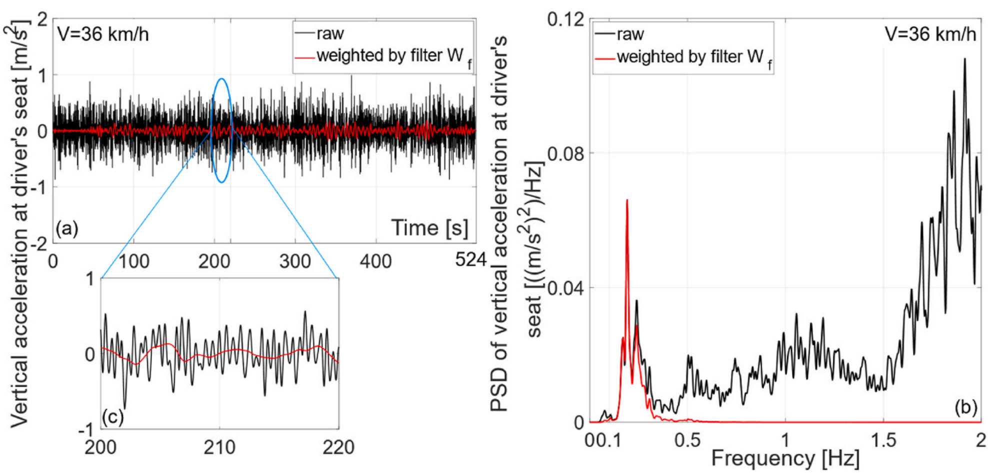

Fig. 19. Raw and frequency weighted vertical acceleration at driver seat surface a) in the time domain; b) in the frequency domain; c) magnified view, for a vehicle velocity of 36 km/h.

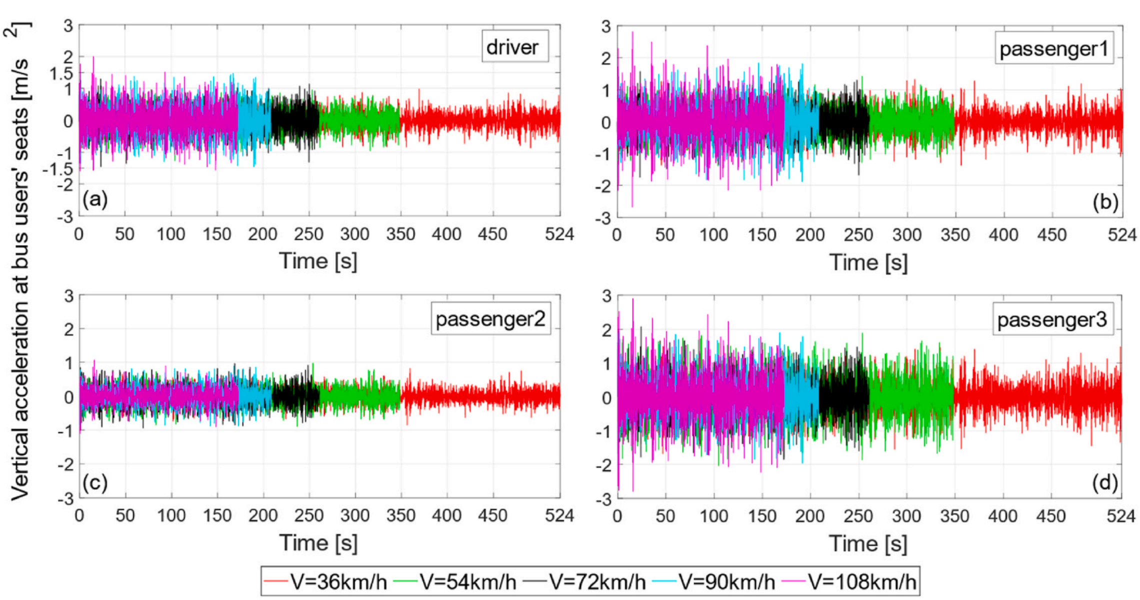

Fig. 20. Vertical acceleration at a) driver seat; b) passenger1 seat; c) passenger2 seat; d) passenger3 seat, as a function of time and vehicle velocity.

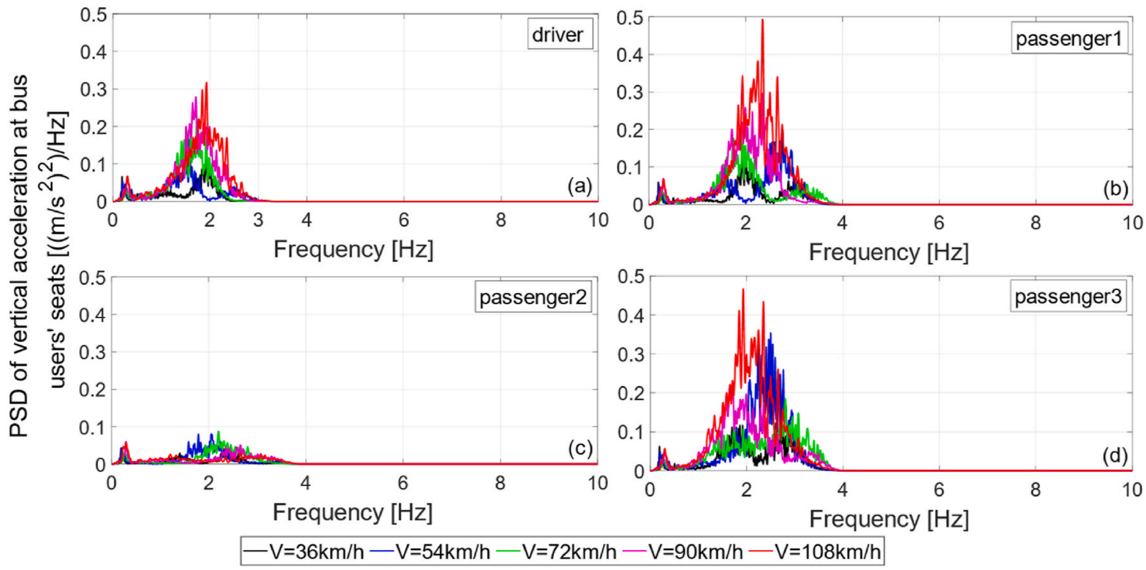

Fig. 21. PSDs of vertical accelerations for a) driver seat; b) passenger1 seat; c) passenger2 seat; d) passenger3 seat, as a function of vehicle velocity.

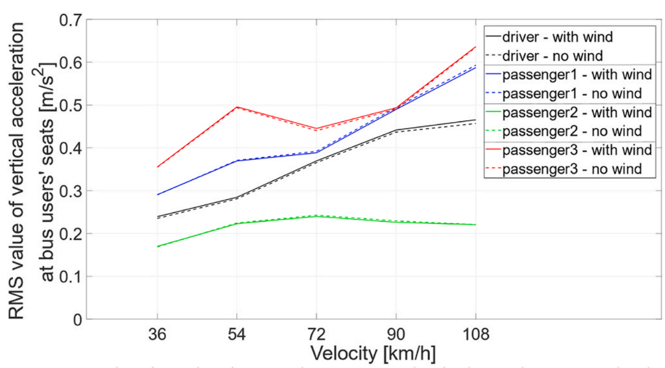

Fig. 22. RMS values of vertical accelerations at bus users' seats with and without wind excitations on the vehicle as a function of vehicle velocity.

5. Simulation results and discussion

This section presents simulation results of characteristic values for 1-year storm conditions, focusing on two cases. The first case considers bridge motions and wind excitations acting on the coach, whereas the second only considers bridge motions. Also, ride comfort and motion sickness have been analysed as a function of storm intensities and vehicle velocity.

5.1. Ride comfort analysis

Fig. 20 shows vertical accelerations acting on bus users from their seats as a function of bus velocity for the first case. It could be noticed that acceleration intensity increases with vehicle velocity for every bus user. Passenger2 is exposed to the lowest vertical acceleration values, whereas passenger3 is exposed to the highest values. For instance, acceleration values acting on passenger2 are in the range of ± 1 m/s^2 (Fig. 20a), whereas for passenger3 in the range of ± 3 m/s^2 (Fig. 20d), for the vehicle velocity of 108 km/h. Despite the driver's suspended seat, the higher vertical acceleration values acting on the driver compared to

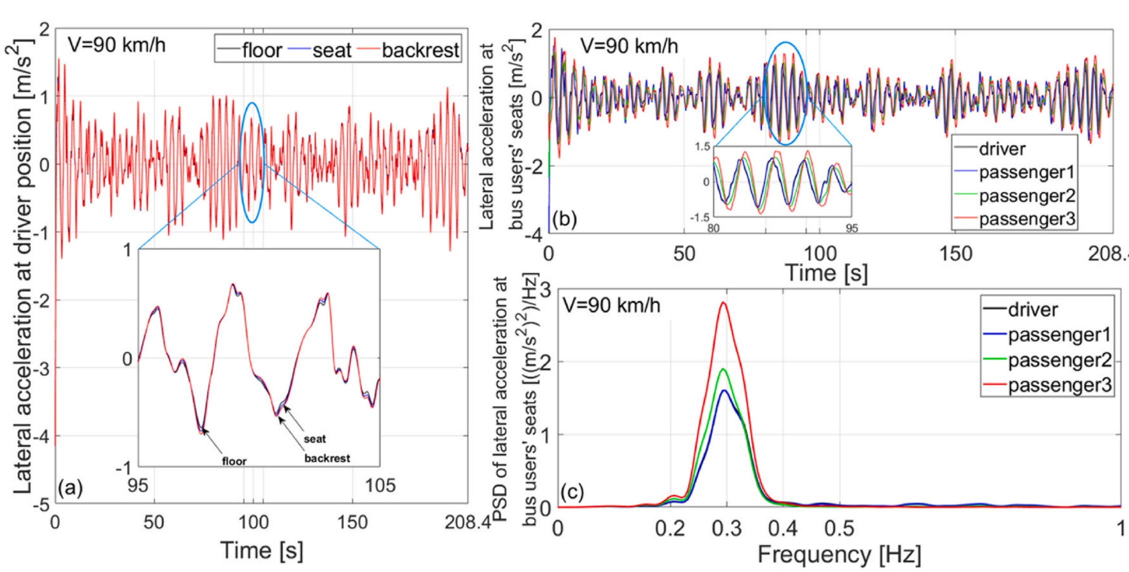

Fig. 23. Lateral accelerations for a) receiving points at driver position; b) at bus users' seats; c) at bus users' seats as a function of frequency.

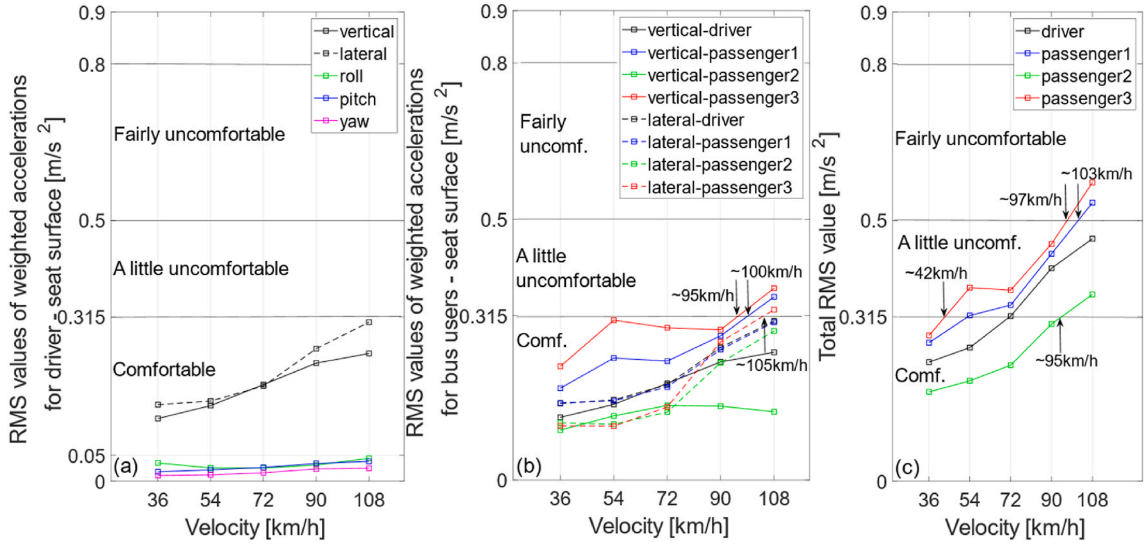

Fig. 24. RMS values a) of the weighted accelerations at the driver's seat; b) of the weighted vertical and lateral accelerations at bus users' seats; c) of total weighted accelerations for bus users, for the case of bridge and wind excitation.

the passenger2 (Fig. 20c) are due to the bus body pitch motion. The effect of the driver's seat in vibration attenuation is noticeable when comparing vertical accelerations acting on the driver and the passenger1. Acceleration values acting on the driver are in the range of ±1.5 m/s^2 (Fig. 20a), whereas for passenger1 they are in the range of ±2 m/s^2 (Fig. 20b), for the vehicle velocity of 108 km/h.

Fig. 21 shows PSDs of bus users' seat vertical acceleration as a function of bus velocity. Acceleration intensity for passengers is concentrated in the frequency range of 0 Hz–4 Hz, whereas for the driver, it is concentrated in the lower frequency range of 0 Hz–3 Hz due to his suspended seat. This is important to notice since the human body is the most sensitive to vertical vibration in a frequency range of 4 Hz–8 Hz (ISO 2631, 1985).

Fig. 22 shows *RMS* values of the vertical acceleration of the bus users' seats for both cases. The wind excitations have an insignificant influence on acceleration intensity.

Fig. 23a shows lateral accelerations at the driver position for different receiving points for the 90 km/h vehicle velocity. It could be seen that backrest acceleration has slightly higher values compared to accelerations from the seat and floor. Fig. 23b presents lateral acceleration from the seat surface for bus users as a function of time. Passenger3 is exposed to the highest values of lateral accelerations. Fig. 23c shows lateral acceleration for bus users in a frequency domain. Acceleration intensities are concentrated in the frequency range 0.2 Hz–0.4 Hz. Peak values at 0.3 Hz correspond to a handwheel steering angle peak frequency at the vehicle velocity of 90 km/h (Sekulic et al., 2021).

Fig. 24 presents *RMS* values of the weighted accelerations for the case of bridge and wind excitations acting on the vehicle when running over the Bjørnafjorden floating bridge. Fig. 24a presents *RMS* values of the weighted accelerations at the driver's seat. Vertical and lateral accelerations are dominant and apparently influence ride comfort the most. *RMS* values of roll, pitch and roll accelerations are small (below 0.05 m/s^2). *RMS* values of the vertical and lateral accelerations are similar up to 72 km/h of vehicle velocity (Fig. 24a). *RMS* values of lateral acceleration are higher than of vertical for the vehicle velocity higher than 72 km/h.

Fig. 24b shows *RMS* values of the weighted vertical and lateral accelerations for every bus user. *RMS* values of the vertical acceleration for

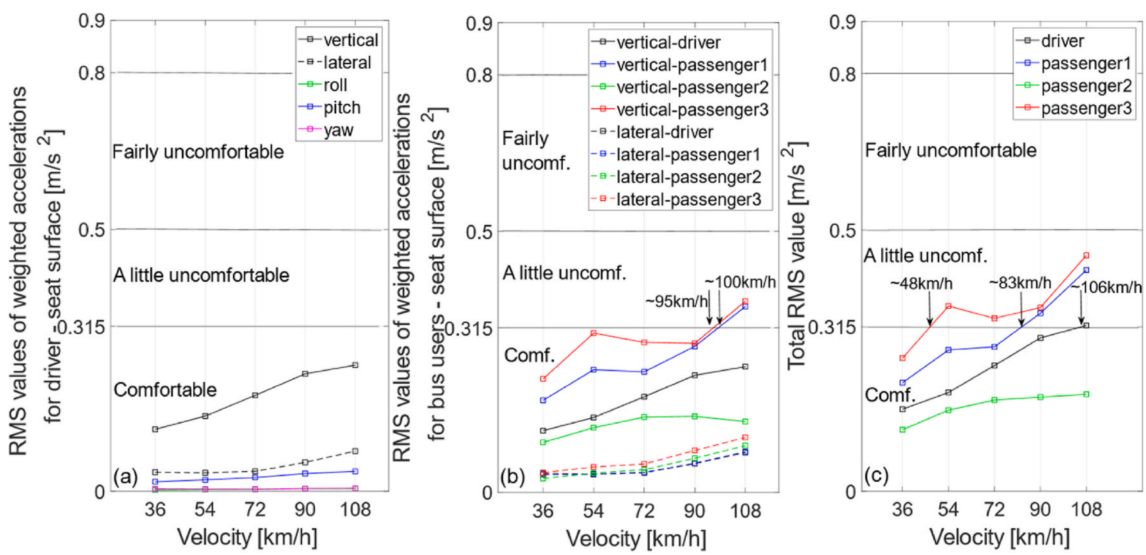

Fig. 25. RMS values a) of the weighted accelerations at the driver's seat; b) of the weighted vertical and lateral accelerations at bus users' seats; c) of total weighted accelerations for bus users, for the case of bridge excitation only.

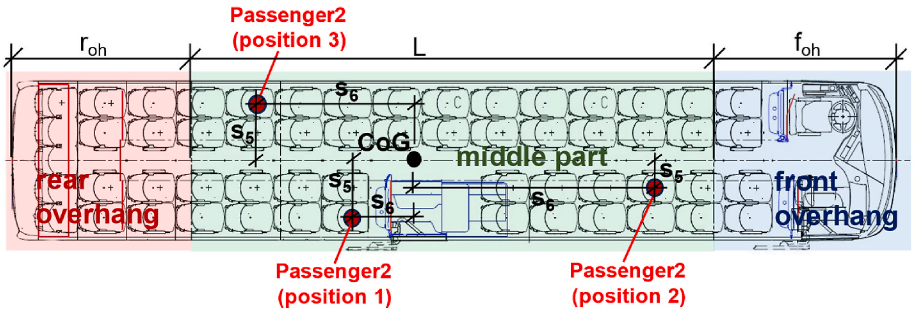

Fig. 26. Different positions of the passenger2's seat in the bus middle part.

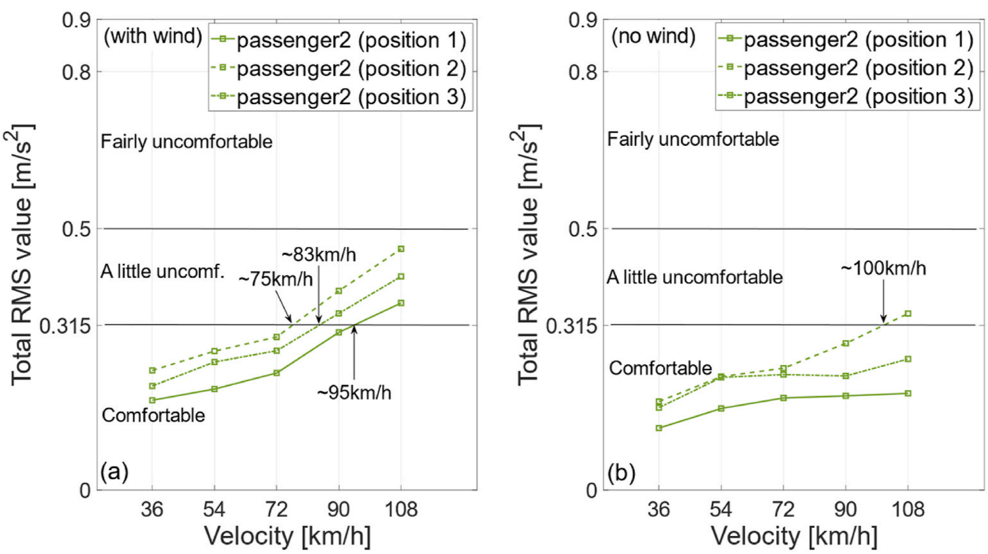

Fig. 27. Total RMS value for different positions of the passenger2's seat in the bus middle part for the case of the a) bridge and wind excitations; b) bridge excitation only.

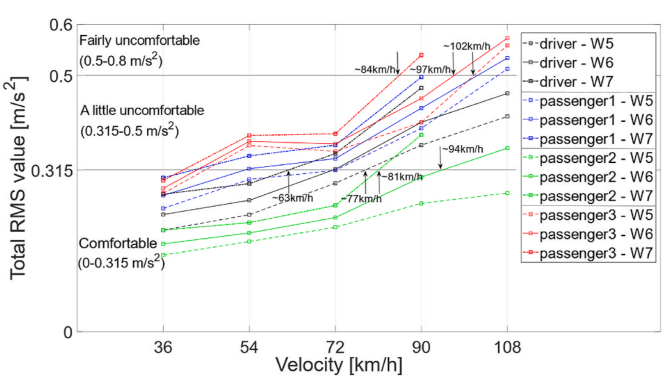

Fig. 28. Total RMS values for the bus users for three storm conditions (W5, W6, W7) as a function of bus velocity.

the passenger3 are the highest. Passenger3 feels *a little uncomfortable* under vertical vibration at the bus velocity of 95 km/h. *RMS* values of the lateral acceleration for the passenger3 increase with the bus velocity. Passenger3 feels *a little uncomfortable* under lateral vibration at the bus velocity of 105 km/h. It could be seen that passenger1 feels *a little uncomfortable* under vertical vibration at the bus velocity of 100 km/h. *RMS* values of the lateral acceleration for passenger1 increase with the bus velocity, however, they are below the limit of 0.315 m/s^2.

Total *RMS* values for bus users are presented in Fig. 24c. At the bus velocity of 42 km/h passenger3 gets *a little uncomfortable*, whereas at a velocity of 97 km/h gets *fairly uncomfortable*. Passenger1 has slightly better ride comfort in comparison to passenger3. At the bus velocity of 54 km/h passenger2 feels *a little uncomfortable*, and at 103 km/h feels *fairly uncomfortable*. At the bus velocity of 72 km/h passenger2 gets *a little uncomfortable*. Passenger2 has the best ride comfort. At the bus velocity of 95 km/h passenger2 gets *a little uncomfortable*.

Fig. 25 presents *RMS* values of the weighted accelerations for the case of floating bridge excitations only acting on the bus when running over it. *RMS* values of the weighted vertical acceleration for the driver are the same as for the first case (Fig. 25a). *RMS* values of the weighted lateral acceleration are considerably lower when compared with the case of the wind excitations acting on the bus (Fig. 25a). *RMS* values of the weighted roll and pitch accelerations are insignificant, whereas the *RMS* value of the pitch acceleration is the same as for the first case (Fig. 25a).

RMS values of weighted lateral accelerations are slightly higher for passenger3, and these values are considerably lower than the 0.315 m/s^2 comfort limit (Fig. 25b). Total *RMS* values for bus users are presented in Fig. 25c. At the bus velocity of 48 km/h, 83 km/h and 106 km/h passenger3, passenger1 and the driver feel *a little uncomfortable*, respectively. Passenger2 feels *comfortable* for every bus speed (Fig. 25c).

Fig. 27 presents ride comfort level for different positions of the passenger2's seat in the bus middle part (Fig. 26). Longitudinal and lateral distances of the passenger2's seat (s_6, s_5) with respect to the bus CoG are denoted in Fig. 27, and the values are given in Table 3.

Fig. 27 presents total *RMS* values as a function of passenger2's seat position for the case of the bridge and wind excitations (Fig. 27a) and for the case of the bridge excitation only (Fig. 27b). At the bus velocity of 95

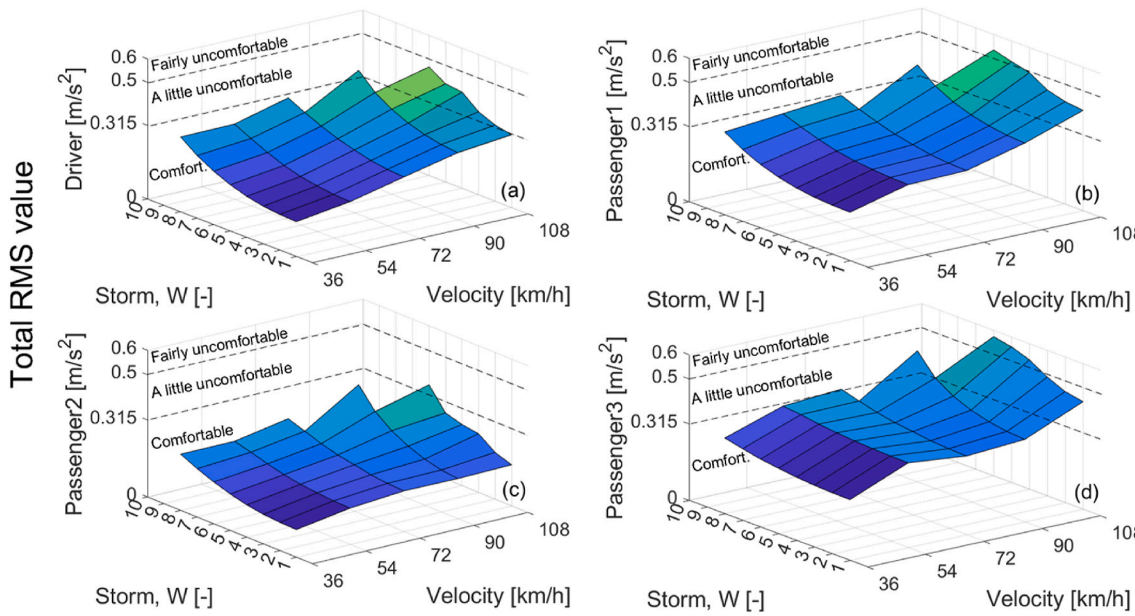

Fig. 29. Total RMS value for a) driver; b) passenger1; c) passenger2; d) passenger3 as a function of storm condition and bus velocity.

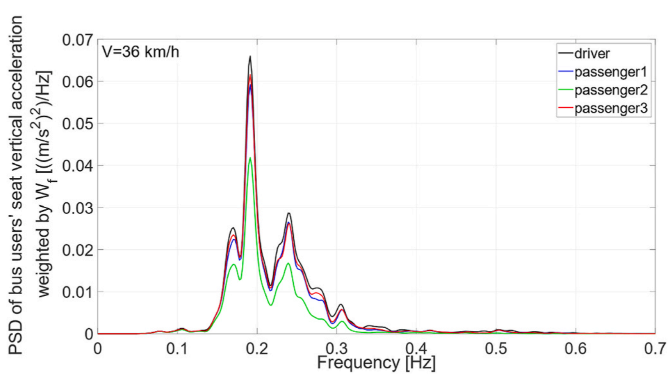

Fig. 30. PSDs of the frequency weighted vertical acceleration by Wf curve for bus users at vehicle velocity of 36 km/h.

km/h, 83 km/h and 75 km/h passenger2 (position 1), passenger2 (position 3) and passenger2 (position 2) feels *a little uncomfortable*, respectively (Fig. 27a). For the case of the bridge excitation only, passenger2 at position 2 (Fig. 26) feels *a little uncomfortable* at the bus speed of 100 km/h (Fig. 27b).

Fig. 28 shows the total *RMS* values of the weighted acceleration for three storm conditions (W5, W6, W7) and every bus user. It can be observed that the bus speed at which the limits of comfort are reached decreases with the intensity of the storm. For example, passenger3 feels *fairly uncomfortable* at bus velocities of 102 km/h, 97 km/h and 84 km/h for storms W5, W6 and W7, respectively. Driver feels *a little uncomfortable* at bus velocities of 77 km/h, 72 km/h and 63 km/h for storms W5, W6 and W7, respectively. Total *RMS* values for storm W7 are not shown in Fig. 28 since the bus is not stable at the velocity of 108 km/h (Sekulic et al., 2023).

Fig. 29 shows total *RMS* values for bus users as a function of storm intensity and coach velocity. Results are not presented for storms more intensive than W8 since the bus was not stable for these conditions (Sekulic et al., 2023). For velocities higher than 54 km/h for W8 and velocity of 108 km/h for W7 bus was also not stable (Sekulic et al., 2023). Passenger2 has the best ride comfort and feels *a little uncomfortable* only for W6 at the bus velocity of 108 km/h (Fig. 29c). Passenger3 has the highest total *RMS* value (Fig. 29d). Passenger3 feels *fairly uncomfortable* for W4 - W6 at a bus speed of 108 km/h (Fig. 29d).

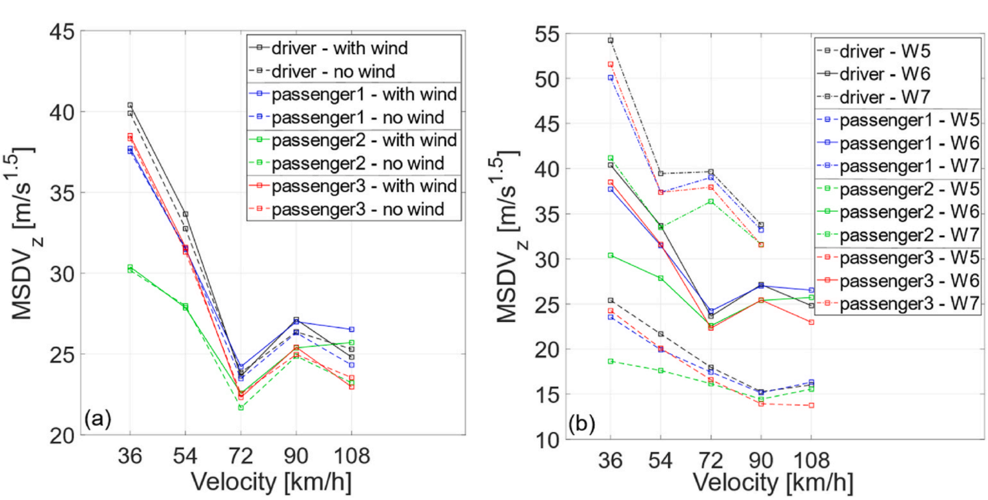

Fig. 31. MSDVz for bus users a) for both cases; b) for three different storm conditions (W5, W6, W7).

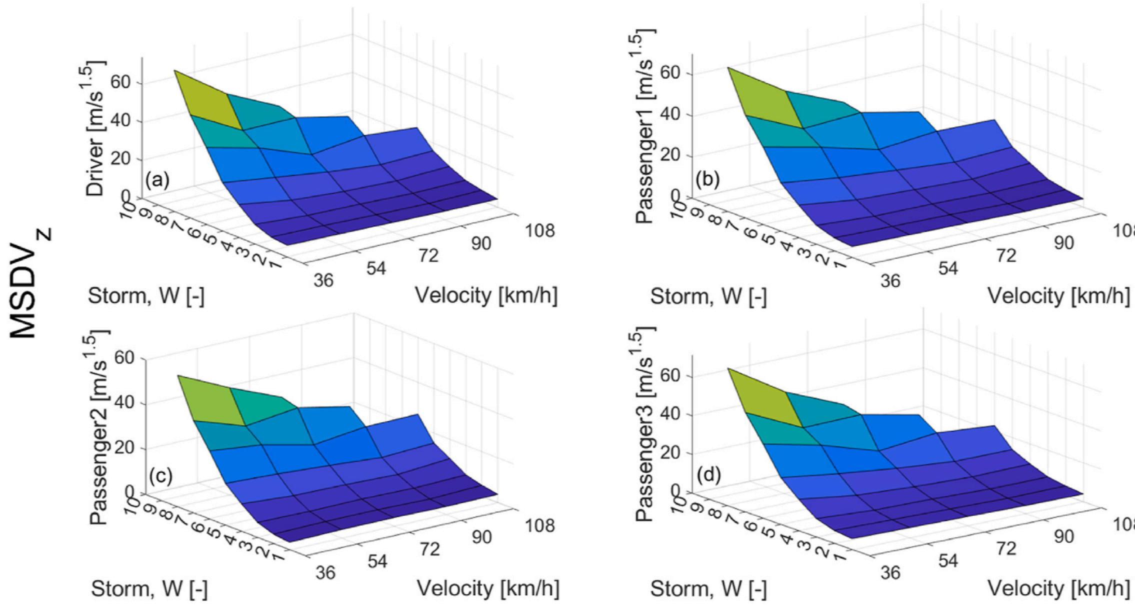

Fig. 32. MSDVz for a) driver; b) passenger1; c) passenger2; d) passenger3, as a function of storm condition and bus velocity.

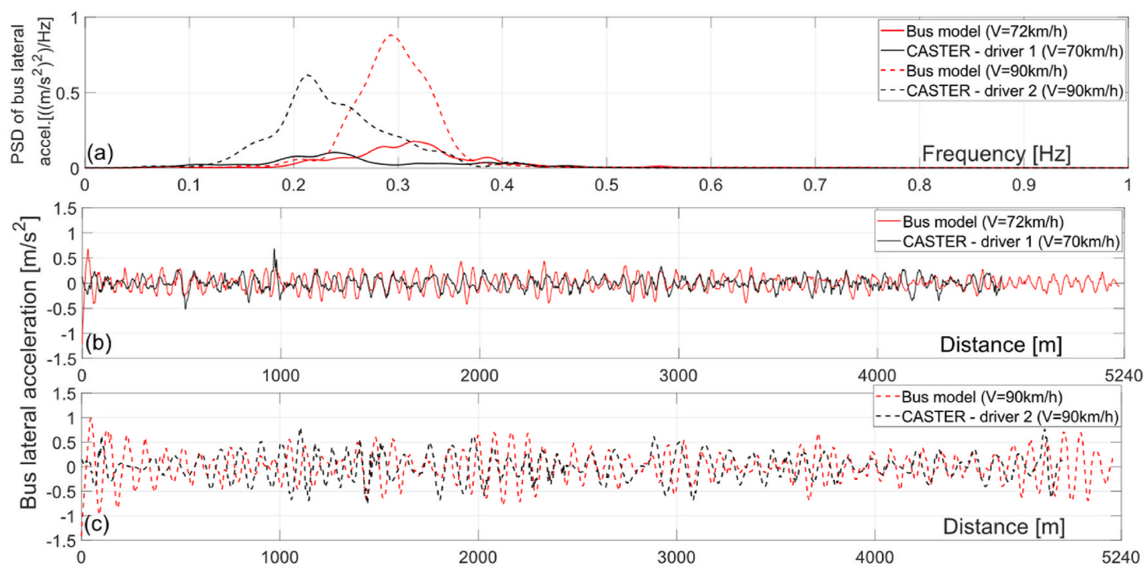

Fig. 33. Bus lateral acceleration signals as a function of a) frequency; b) distance for vehicle speed of 70 km/h (driver 1); c) distance for vehicle speed of 90 km/h (driver 2).

5.2. Motion sickness analysis

Fig. 30 shows frequency-weighted vertical accelerations by filter W_f (Fig. 17) for bus users' seats at the vehicle velocity of 36 km/h. Acceleration intensities are found in the frequency range 0.1 Hz–0.4 Hz. The acceleration peak at around 0.2 Hz corresponds to the peak of vertical bridge motion due to wave excitation (Sekulic et al., 2023). It could be noticed that acceleration intensities are the highest for the bus driver, and the lowest for passenger2.

Fig. 31a shows *MSDVz* calculated for bus users for both cases as a function of vehicle velocity. Wind load has an insignificant influence on *MSDVz*. *MSDVz* decreases with vehicle velocity up to 72 km/h. The highest value of *MSDVz* for every user is achieved for the lowest bus speed of 36 km/h due to the longest time of vibrational exposure. Among bus users, the driver is the most likely to feel motion sickness on a floating bridge due to his suspended seat. Fig. 31b presents *MSDVz* for bus users for three storm conditions (W5, W6 and W7). *MSDVz* increases with storm intensity with similar characteristic changes as a function of vehicle velocity.

Fig. 32 shows *MSDVz* for bus users as a function of storm conditions and vehicle velocity. For every bus user, a greater incidence of motion sickness happens in lower vehicle velocity and stronger storms. For example, for vehicle speed of 36 km/h and storm W8, *MSDVz* is over 50 $m/s^{1.5}$ for bus driver (Fig. 32a). Passenger2 is less likely to feel motion sickness (Fig. 32c).

6. BUS model Validation

Validation of the bus mathematical model has been done by comparing two signals (bus lateral acceleration and bus roll angle) from driving simulator tests and numerical simulations for W6 (1-year storm condition). The Hexatech 1CTR driver-in-the-loop motion platform

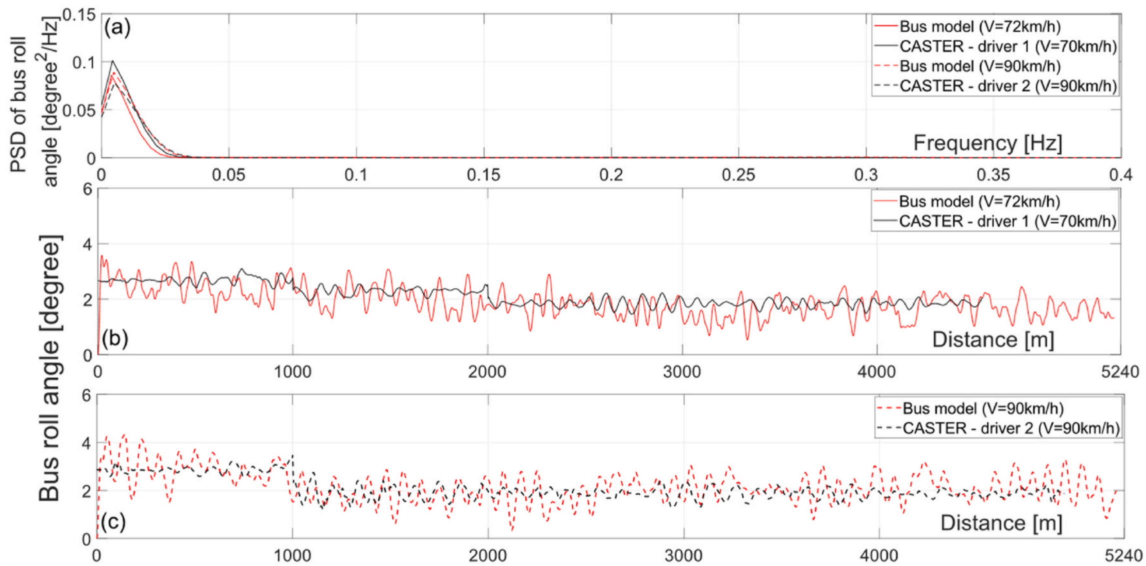

Fig. 34. Bus roll angle as a function of a) frequency; b) distance for vehicle speed of 70 km/h (driver 1); c) distance for vehicle speed of 90 km/h (driver 2).

simulator (CASTER) has been previously used for the investigation of vehicles (passenger car/bus) tracking ability and driver behaviour on Bjørnafjorden floating bridges (Bhat et al., 2020).

Fig. 33 comparatively shows bus lateral accelerations from driving simulator tests (two drivers) and from numerical simulations for two vehicle speeds of 70 km/h (driver 1) and 90 km/h (driver 2). The magnitudes of signals are similar (Fig. 33(b and c)). In the frequency domain, signal intensities for driver 1 and driver 2 are concentrated at approximately 0.25 Hz whereas for the bus model around 0.3 Hz (Fig. 33a). However, frequency ranges of lateral accelerations from driving simulator tests and numerical simulations are fairly matched (Fig. 33a).

Fig. 34 comparatively shows bus roll angle responses from driving simulator tests (two drivers) and from numerical simulations for two vehicle speeds of 70 km/h (driver 1) and 90 km/h (driver 2). The magnitudes from driving tests are lower compared to numerical simulations (Fig. 34(b and c)), but with similar trend. Values of the bus roll angle decrease with distance for both driving tests and simulations due to the higher values of cross wind component on the first 1000 m of travelled distance (Fig. 15b). Signal intensities are concentrated at low frequency range (below 0.05 Hz, Fig. 34a) which correspond to the cross-wind component frequency range (Sekulic et al., 2021, 2022).

7. Conclusion

This work investigated the vibrational influence of Bjørnafjorden floating bridge motions and wind excitations on bus users' ride comfort and motion sickness. Two cases were considered for 1-year storm condition – the first case with the wind loads affecting the bus, and the second case with no wind loads affecting the bus. Furthermore, storm conditions of higher and lower intensity than 1-year storm were considered in the analysis.

From this paper, the main conclusions are as follows.

- Vertical vibration intensity increases with vehicle velocity for every bus user. The passenger at the bus's rear overhang is exposed to the highest vertical accelerations, and the passenger in the bus's middle part is exposed to the lowest.
- Wind excitations insignificantly influence vertical and pitch vibration from bus users' seats. Wind excitations considerably influence lateral, yaw and roll accelerations acting on bus users' bodies.
- For the first case, *RMS* values of the vertical and lateral weighted accelerations for the driver seat are similar up to 72 km/h of vehicle velocity. For the bus velocity higher than 72 km/h, *RMS* values of lateral acceleration are dominant.
- For the second case, the *RMS* values of the vertical weighted accelerations are considerably higher than the lateral accelerations for the driver seat.
- For both cases, for passengers seating on the seats at the front and the rear bus overhang, a comfort limit of 0.315 m/s^2 (*a little uncomfortable*) could be reached by only vertical vibration from their seats at a velocity of 100 km/h (for the front seat) and 95 km/h (for the rear seat).
- For the first case, a comfort limit of 0.315 m/s^2 is reached for the driver, for the passenger at the front, for the passenger at the middle and for the passenger at the rear part of the bus at velocity of 72 km/h, 54 km/h, 95 km/h and 42 km/h, respectively. A comfort limit of 0.5 m/s^2 (*fairly uncomfortable*) is reached for the passenger at the front and for the passenger at the rear of the bus at a velocity of 103 km/h and 97 km/h, respectively.
- For the second case, a comfort limit of 0.315 m/s^2 is reached for the driver, the passenger at the front and the passenger at the rear at bus velocities of 106 km/h, 83 km/h and 48 km/h, respectively. A passenger in the middle part feels comfortable regardless of the considered bus's velocity.
- The bus velocity at which the limits of comfort are reached decreases with the intensity of the storm. For example, passenger3 feels *fairly uncomfortable* at the bus velocities of 102 km/h, 97 km/h and 84 km/h for storms W5, W6 and W7, respectively.
- Among bus users, passenger2 has the best ride comfort, and passenger3 has the highest total *RMS* value and apparently the worst ride comfort. Vehicle velocities at which ride comfort limit of 0.315 m/s^2 (*a little uncomfortable*) is reached decrease with increasing distance from the passenger2's seat to the bus CoG.
- Wind load on a bus has an insignificant influence on *MSDVz*. The highest value of *MSDVz* for every user is achieved for the lowest bus speed of 36 km/h due to the longest time of vibrational exposure.
- Among bus users, the driver is the most likely to feel motion sickness on the floating bridge. Unlike ride comfort, the driver's suspended seat negatively influences his motion sickness.

One of the potential solutions for vibration mitigation could be to propose new values of oscillatory parameters for passenger seats that do not provide a satisfactory level of oscillatory comfort (e.g. passenger1, passenger3).

The Bjørnafjorden floating bridge is part of the coastal highway route E39 Norway's road project and is currently in its design phase. Therefore, experimental investigation of the vehicle's behaviour and verification of the validity of vehicle models on the Bjørnafjorden floating bridge are planned for future work. In addition, measurement of floating bridge motion and crosswind speed along the length of the bridge are planned as future work.

CRediT authorship contribution statement

Dragan Sekulic: Writing – original draft, Visualization, Methodology, Data curation, Conceptualization. **Alexey Vdovin:** Supervision, Conceptualization. **Bengt Jacobson:** Supervision, Methodology, Conceptualization. **Simone Sebben:** Supervision, Conceptualization. **Stian Moe Johannesen:** Resources, Investigation.

Declaration of competing interest

The authors declare that they have no known competing financial interests or personal relationships that could have appeared to influence the work reported in this paper.

Acknowledgements

Support for this research was provided by The Norwegian Public Roads Administration (NPRA). This support is gratefully acknowledged.

The computations were enabled by resources provided by the National Academic Infrastructure for Supercomputing in Sweden (NAISS) and the Swedish National Infrastructure for Computing (SNIC) at the National Supercomputer Centre (NSC) and Chalmers' Centre for Computational Science and Engineering (C3SE) partially funded by the Swedish Research Council through grant agreements no. 2018–05973 and no. 2022–06725.

A group of master students should also be acknowledged, as their work helped to develop the models and simulate for numerous conditions and prepare for future studies involving motion platform driving simulators, see http://hdl.handle.net/20.500.12380/307536.

Appendix

Table 3
Coach parameters

Geometric parameters of the bus	
Wheelbase L [m]	8.375
Front overhang f_{oh} [m]	2.619
Rear overhang r_{oh} [m]	2.806
Distance from the front axle to the centre of gravity (CoG) of an empty bus l_f [m]	4.4103
Distance from the rear axle to the centre of gravity (CoG) of empty bus l_r [m]	3.9647
Distance from the front right/left wheel to the front axle CoG b_f [m]	1.00
Distance from the rear right/left wheel to the rear axle CoG b_r [m]	1.00
Distance from the CoG of the whole vehicle to the ground $h_{CoG,\ stat.}$ [m]	1.1725
Height of the front axle roll-centre $h_{RCfa,\ stat.}$ [m]	0.508
Height of the rear axle roll-centre $h_{RCra,\ stat.}$ [m]	0.508
Distance from the CoG to the roll-centre for the front axle $h_{RCfa,\ stat.}$ [m]	0.6645
Distance from the CoG to the roll-centre for the rear axle $h_{RCra,\ stat.}$ [m]	0.6645
Distance from suspension elements on the front axle to the front axle CoG e_{u1} [m]	0.70
Distance from suspension elements on the rear axle to the rear axle CoG e_{u2} [m]	0.80
Position of the bus users' receiving points	
Distance from the driver seat to the vehicle x-axis s_1 [m]	0.65
Distance from the driver seat to the vehicle y-axis s_2 [m]	5.9103
Distance from passenger1 seat to the vehicle x-axis s_3 [m]	0.80
Distance from passenger1 seat to the vehicle y-axis s_4 [m]	5.2103
Distance from passenger2 (position 1) seat to the vehicle x-axis s_5 [m]	0.80
Distance from passenger2 (position 1) seat to the vehicle y-axis s_6 [m]	0.50
Distance from passenger2 (position 2) seat to the vehicle x-axis s_5 [m]	0.50
Distance from passenger2 (position 2) seat to the vehicle y-axis s_6 [m]	3.80
Distance from passenger2 (position 3) seat to the vehicle x-axis s_5 [m]	0.80
Distance from passenger2 (position 3) seat to the vehicle y-axis s_6 [m]	2.28
Distance from passenger3 seat to the vehicle x-axis s_7 [m]	0.40
Distance from passenger3 seat to the vehicle y-axis s_8 [m]	5.4647
Vertical distance between floor at driver position and CoG $h_{d,f}$ [m]	0.10
Vertical distance between seat at driver position and CoG $h_{d,s}$ [m]	0.50
Vertical distance between backrest at driver position and CoG $h_{d,b}$ [m]	0.80
Vertical distance between floor at passenger1/2/3 position and CoG $h_{p1/2/3,f}$ [m]	0.30
Vertical distance between seat at passenger1/2/3 position and CoG $h_{p1/2/3,s}$ [m]	0.70
Vertical distance between backrest at passenger1/2/3 position and CoG $h_{p1/2/3,b}$ [m]	1.00
Mass parameters of the bus	
Driver and seat - mass m_d [kg]	100
Passenger1 and seat - mass m_{p1} [kg]	90
Passenger2 and seat - mass m_{p2} [kg]	90
Passenger3 and seat - mass m_{p3} [kg]	90
Sprung mass of the empty bus m_s [kg]	16099
Front axle - mass m_{u1} [kg]	746
Rear axle - mass m_{u2} [kg]	1355
Empty bus - mass m [kg]	18200

(*continued on next page*)

Table 3 (*continued*)

Sprung mass - moment of inertia about its x-axis J_{sx} [kgm^2]	33400
Sprung mass - moment of inertia about its y-axis J_{sy} [kgm^2]	150000
Bus - moment of inertia about z-axis J_z [kgm^2]	290000
Front axle - moment of inertia relative to the x_1-axis J_{ux1} [kgm^2]	315
Rear axle - moment of inertia relative to the x_2-axis J_{ux2} [kgm^2]	657
Oscillatory parameters of the bus	
Spring stiffness of the driver seat suspension system k_d [N/m]	7500
Shock-absorber damping of the driver seat suspension system c_d [Ns/m]	750
Stiffness of the passenger1, passenger2 and passenger3 seats k_{p1}, k_{p2}, k_{p3} [N/m]	40000
Damping of the passenger1, passenger2 and passenger3 seats c_{p1}, c_{p2}, c_{p3} [Ns/m]	220
Stiffness for one air spring on the front axle k_{sf} [N/m]	175000
Stiffness for all air springs on the front axle k_{sfeq} [N/m]	350000
Damping for one shock-absorber on the front axle c_{df} [Ns/m]	20000
Damping for all shock-absorbers on the left side of the front axle c_{dfl} [Ns/m]	40000
Damping for all shock-absorbers on the right side of the front axle c_{dfr} [Ns/m]	40000
Damping for all shock-absorbers on the front axle c_{dfeq} [Ns/m]	80000
Stiffness for one air spring on the rear axle k_{sr} [N/m]	200000
Stiffness for all air springs on the left side of the rear axle k_{srl} [N/m]	400000
Stiffness for all air springs on the right side of the rear axle k_{srr} [N/m]	400000
Stiffness for all air springs on the rear axle k_{sreq} [N/m]	800000
Damping for one shock-absorber on the rear axle c_{dr} [Ns/m]	22500
Damping for all shock-absorbers on the left side of the rear axle c_{drl} [Ns/m]	45000
Damping for one shock-absorber on the right side of the rear axle c_{drr} [Ns/m]	45000
Damping for all shock-absorbers on the rear axle c_{dreq} [Ns/m]	90000
Radial stiffness for one tyre on the left/right side of the front axle k_{tfl}/k_{tfr} [N/m]	1000000
Radial stiffness for all tyres on the front axle k_{tfeq} [N/m]	2000000
Radial stiffness for one tyre on the left/right side of rear axle k_{trl}/k_{trr} [N/m]	2000000
Radial stiffness for all tyres on the rear axle k_{treq} [N/m]	4000000
Torsional stiffness for anti-roll bar on front axle K_{arbf} [Nm/rad]	120000
Torsional stiffness for anti-roll bar on rear axle K_{arbr} [Nm/rad]	120000
Front axle - roll-stiffness $K_{\varphi f}$ [Nm/rad]	171500
Front axle - roll-damping $C_{\varphi f}$ [Nms/rad]	39200
Rear axle - roll-stiffness $K_{\varphi r}$ [Nm/rad]	512000
Rear axle - roll-damping $C_{\varphi r}$ [Nms/rad]	57600

Table 4
Other notations

O_1xyz	Vehicle coordinate system
Δ	Steering angle for front vehicle left/right wheel [rad]
φ_s, φ_1, φ_2	Roll-angle motion for the vehicle body, front axle, and rear axle [rad]
ω_s, ω_1, ω_2	Roll-angle rate for the vehicle body, front axle, and rear axle [rad/s]
$\dot{\omega}_s$, $\dot{\omega}_1$, $\dot{\omega}_2$	Roll-angle acceleration for the vehicle body, front axle, and rear axle [rad/s^2]
θ_s, $\dot{\theta}_s$, $\ddot{\theta}^s$	Pitch-angle motion rate and acceleration for the vehicle body [rad], [rad/s], [rad/s^2]
z, $\dot{z}$, $\ddot{z}$	Vertical motion/velocity/acceleration of the vehicle body [m; m/s; m/s^2]
z_1, $\dot{z}_1$, $\ddot{z}_1$	Vertical motion/velocity/acceleration of the coach front axle [m; m/s; m/s^2]
z_2, $\dot{z}_2$, $\ddot{z}_2$	Vertical motion/velocity/acceleration of the coach rear axle [m; m/s; m/s^2]
z_d, $\dot{z}_d$, $\ddot{z}_d$	Vertical motion/velocity/acceleration of the coach diver [m; m/s; m/s^2]
z_{p1}, $\dot{z}_{p1}$, $\ddot{z}_{p1}$	Vertical motion/velocity/acceleration of the passenger1 [m; m/s; m/s^2]
z_{p2}, $\dot{z}_{p2}$, $\ddot{z}_{p2}$	Vertical motion/velocity/acceleration of the passenger2 [m; m/s; m/s^2]
z_{p3}, $\dot{z}_{p3}$, $\ddot{z}_{p3}$	Vertical motion/velocity/acceleration of the passenger3 [m; m/s; m/s^2]
$\dot{v}_y$	Lateral acceleration of the coach CoG in vehicle fixed coordinate system [m/s^2]
a_y	Total lateral acceleration of the coach CoG in vehicle fixed coordinate system [m/s^2]
v_x, v_y	Longitudinal/lateral velocity of the coach CoG in vehicle fixed coordinate system [m/s]
Ψ, ω_z, $\dot{\omega}_z$	Vehicle yaw motion/rate/acceleration [rad; rad/s; rad/s^2]
ζ_{tfr}, ζ_{tfl}	Vertical excitations on the front right/left wheel
ζ_{trr}, ζ_{trl}	Vertical excitations on the rear right/left wheel
ζ_{fa}, ζ_{ra}	Road roughness below front/rear axle CoGs
ζ_1	Road roughness below the rotational centre of sprung mass (*RC*)
$v_{y\ br,fa}$, $v_{y\ br,ra}$	Lateral velocity of the bridge deck at the tyre contact point for the front/rear coach axle [m/s]
Δh_{sm}	Vertical distance from CoG to vehicle roll-axis (point *RC*) [m]

Table 5
Multiplying factors for RMS values of frequency-weighted accelerations (ISO 2631/1997)

Multiplying factors	
Floor – vertical $k_{z,floor}$ [-]	0.40
Floor – lateral $k_{y,floor}$ [-]	0.25
Seat – vertical $k_{z,seat}$ [-]	1.00

(*continued on next page*)

Table 5 (*continued*)

Multiplying factors	
Seat – lateral $k_{y,seat}$ [-]	1.00
Seat – roll $k_{roll,\ seat}$ [m/rad]	0.63
Seat – pitch $k_{pitch,\ seat}$ [m/rad]	0.40
Seat – yaw $k_{yaw,\ seat}$ [m/rad]	0.20
Backrest – vertical $k_{z,seat\text{-}back}$ [-]	0.40
Backrest – lateral $k_{y,seat\text{-}back}$ [-]	0.50

Data availability

Data will be made available on request.

References

Alperovitch-Najenson, D., Santo, Y., Masharawi, Y., Katz-Leurer, M., Ushvaev, D., Kalichman, L., 2010. Low back pain among professional bus drivers: ergonomic and occupational-psychosocial risk factors. Isr. Med. Assoc. J. 12 (1), 26–31. PMID: 20450125.

Aslan, S., Ozgur, K., Yavuz, K., Hayati, K., Naci, E., Ozlem, B., 2005. Speed bump-induced spinal column injury. Am. J. Emerg. Med. 23 (4), 563–564. https://doi.org/10.1016/j.ajem.2004.12.015.

Barabino, B., Eboli, L., Mazzulla, G., Mozzoni, S., Murru, R., Pungillo, G., 2019. An innovative methodology to define the bus comfort level. Transp. Res. Procedia 41, 461–470. https://doi.org/10.1016/j.trpro.2019.09.077.

Bhat, A.B., et al., 2020. Driver influence on vehicle track-ability on floating bridges. TME180 Automotive Engineering Project. Chalmers University of Technology, Gothenburg, Sweden. https://odr.chalmers.se/handle/20.500.12380/300748.

Blood, R.P., Ploger, J.D., Yost, M.G., Ching, R.P., Johnson, P.W., 2010. Whole body vibration exposures in metropolitan bus drivers: a comparison of three seats. J. Sound Vib. 329 (1), 109–120. https://doi.org/10.1016/j.jsv.2009.08.030.

Bowrey, D., Thomas, R., Evans, R., Richmond, P., 1996. Road humps: accident prevention or hazard? J. Accid. Emerg. Med. 13 (4), 288–289. https://doi.org/10.1136/emj.13.4.288.

Branlard, E., 2010. Wind Energy: Generation of Time Series from a Spectrum. Technical University of Denmark, Denmark.

ISO 2631, 1985. Evaluation of Human Exposure to Whole-Body Vibration: Part 1 -General Requirements. International Organization for Standardization, Geneva)">.

ISO 2631, 1997. Mechanical Vibration and Shock: Evaluation of Human Exposure to Whole-Body Vibration - Part 1: General Requirements. International Organization for Standardization, Geneva.

Jacobson, B., 2020. Vehicle Dynamics Compendium. Chalmers University of Technology. https://research.chalmers.se/publication/513850/file/513850_Fulltext.pdf.

Juhlin, M., 2009. Assessment of Crosswind Performance of Buses. KTH. PhD Thesis. https://www.diva-portal.org/smash/get/diva2:216431/FULLTEXT01.pdf.

Patterson, P.K., Eubanks, T.L., Ramseyer, R., 1986. Back discomfort prevalence and associated factors among bus drivers. AAOHN J. 34 (10), 481–484. https://doi.org/10.1177/216507998603401004.

Rana, S., Asaduzzaman, 2021. Vibration based pavement roughness monitoring system using vehicle dynamics and smartphone with estimated vehicle parameters. Results Eng 12, 100294. https://doi.org/10.1016/j.rineng.2021.100294.

Sekulic, D., Dedovic, V., Rusov, S., Salinic, S., Obradovic, A., 2013. Analysis of vibration effects on the comfort of intercity bus users by oscillatory model with ten degrees of freedom. Appl. Math. Model. 37 (18), 8629–8644. https://doi.org/10.1016/j.apm.2013.03.060.

Sekulic, D., Dedovic, V., Rusov, S., Obradovic, A., Salinic, S., 2016. Definition and determination of the bus oscillatory comfort zones. Int. J. Ind. Ergon. 53, 328–339. https://doi.org/10.1016/j.ergon.2016.04.003.

Sekulic, D., Vdovin, A., Jacobson, B., Sebben, S., Johannesen, S., 2021. Effects of wind loads and floating bridge motion on intercity bus lateral stability. J. Wind Eng. Ind. Aerod. 212, 104589. https://doi.org/10.1016/j.jweia.2021.104589.

Sekulic, D., Vdovin, A., Jacobson, B., Sebben, S., Johannesen, S., 2022. Analysis of vehicles path tracking ability and lateral stability on a floating bridge under crosswind. J. Wind Eng. Ind. Aerod. 227, 105070. https://doi.org/10.1016/j.jweia.2022.105070.

Sekulic, D., Vdovin, A., Jacobson, B., Sebben, S., Johannesen, S., 2023. Determination of safe speeds for a coach travelling on a floating bridge. Transp. Res. Interdiscip. Perspect.

Shen, X., Feng, S., Li, Z., Hu, B., 2016. Analysis of bus passenger comfort perception based on passenger load factor and in - vehicle time. SpringerPlus 62 (6), 1–10. https://doi.org/10.1186/s40064-016-1694-7.

Vegvesen, 2017. SBJ-31-C3-MUL-22-RE-100 - Bjørnafjorden, Straight Floating Bridge Phase 3 - Analysis and Design (Base Case).

Vegvesen, N400 Bruprosjektering, 2015. Prosjektering Av Bruer, Ferjekaier Og Andre.

William, Y., Oraby, W., Metwally, S., 2014. Analysis of vehicle lateral dynamics due to variable wind gusts. SAE Int. J. Commer. Veh. 7 (2), 666–674. https://doi.org/10.4271/2014-01-2449.

Zhou, Y., Chen, S., 2016. Vehicle ride comfort analysis with whole-body vibration on long-span bridges subjected to crosswind. J. Wind Eng. Ind. Aerod. 155, 126–140. https://doi.org/10.1016/j.jweia.2016.05.001.

Zhu, J., Zhang, W., Wu, M.X., 2018. Evaluation of ride comfort and driving safety for moving vehicles on slender coastal bridges. J. Vib. Acoust. 140 (5), 051012. https://doi.org/10.1115/1.4039569.

Zhu, J., Xiong, Z., Xiang, H., Huang, X., Li, Y., 2021. Ride comfort evaluation of stochastic traffic flow crossing long-span suspension bridge experiencing vortex-induced vibration. J. Wind Eng. Ind. Aerod. 219, 104794. https://doi.org/10.1016/j.jweia.2021.104794.